Fermi National Accelerator Laboratory

FERMILAB-Pub-94/085

Accelerator/Experiment Interface at Hadron Colliders: Energy Deposition in the IR Components and Machine Related Background to Detectors

N. Mokhov

Fermi National Accelerator Laboratory
P.O. Box 500, Batavia, Illinois 60510

April 1994

Submitted to the *Journal of Nuclear Instruments and Methods in Physics Research*

Operated by Universities Research Association Inc. under Contract No. DE-AC02-76CHO3000 with the United States Department of Energy

Disclaimer

This report was prepared as an account of work sponsored by an agency of the United States Government. Neither the United States Government nor any agency thereof, nor any of their employees, makes any warranty, express or implied, or assumes any legal liability or responsibility for the accuracy, completeness, or usefulness of any information, apparatus, product, or process disclosed, or represents that its use would not infringe privately owned rights. Reference herein to any specific commercial product, process, or service by trade name, trademark, manufacturer, or otherwise, does not necessarily constitute or imply its endorsement, recommendation, or favoring by the United States Government or any agency thereof. The views and opinions of authors expressed herein do not necessarily state or reflect those of the United States Government or any agency thereof.

FERMILAB-Pub-94/.....-

Accelerator/Experiment Interface at Hadron Colliders: Energy Deposition in the IR Components and Machine Related Background to Detectors

N. Mokhov

Fermi National Accelerator Laboratory
P.O. Box 500, Batavia, Illinois 60510

April 1994

Submitted to the *Journal of Nuclear Instruments and Methods in Physics Research.*

Accelerator/Experiment Interface at Hadron Colliders: Energy Deposition in the IR Components and Machine Related Background to Detectors

N. Mokhov

Fermi National Accelerator Laboratory
P.O. Box 500, Batavia, Illinois 60510

Abstract

At superconducting hadron colliders such as SSC, LHC, and upgraded Tevatron, the mutual effect of the radiation environment produced by the accelerator and experiments is one of the key issues in the interaction region and detector development. In this work comprehensive studies were performed on beam induced energy deposition, radiation effects and particle background in the SSC low-beta interaction regions. The DTUJET92 code is used to generate 20×20 TeV pp-events. Hadronic and electromagnetic cascades, and neutron transport down to thermal energies in the accelerator and detector components, tunnel and experimental halls are simulated with the MARS12 Monte Carlo code. The detailed lattice and magnet parameters, all important SDC and GEM detectors features in the near-beam region as well as tunnel and experimental hall geometry and materials are taken into account. Calculations were performed for a few detector-free spaces. Energy and luminosity dependencies of the obtained results are discussed as well as efficiencies of some proposed protective measures. Most of the results of this paper are directly applicable to the LHC and various scenarios of the Tevatron upgrade, as well as to the future e^+e^- linear colliders.

CONTENTS

1. Introduction

The Superconducting Super Collider (SSC) was designed to usher in the next generation of hadron colliders. Two proton beams with 20 TeV energy each would allow a peak luminosity of up to 10^{33} cm^2 s^{-1} at 2 to 4 interaction regions (IR) with the possibility to upgrade to 10^{34} cm^{-2}s^{-1}. Two general purpose detectors, SDC and GEM, proposed to be located at low-β IRs, were aimed at pursuing a broad range of physics goals and were designed to accomodate an inelastic interaction rate of 10^8 s^{-1} or even 10^9 s^{-1} (with somewhat reduced functionality). At the above rate mutual effect of the radiation environment produced by the accelerator and experiments became one of the key issues in the interaction region and detector development. High radiation levels in and around the final focus triplet quadrupoles, IR superconducting dipoles, the neutral beam dump, the detectors themselves and experimental halls, forced a special approach to the design of these components and of the whole region [1].

In the present paper results of comprehensive studies on beam-induced energy deposition, radiation effects and particle background in the SSC low-β interaction regions are described. The DTUJET92 code [2], based on the dual topological unitarization model for hadronic multi-particle production, is used to generate 20 × 20 TeV *pp*-events. Hadronic and electromagnetic cascades, and neutron transport down to thermal energies in the accelerator and detector components, tunnel and experimental halls are simulated with the MARS12 Monte Carlo code [3]. The detailed lattice and magnet parameters, all important SDC and GEM detectors features in the near-beam region, as well as tunnel and experimental hall geometry and materials are taken into account. Calculations are performed for ±20.5, ± 25, and ± 35 m detector-free spaces. The effect of implementation of the proposed protective measures is described. Energy and luminosity dependencies of the results are discussed through the text. Most of this paper is directly applicable to LHC and various scenarios of the Tevatron upgrade, as well as to e^+e^- linear colliders like TESLA.

2. Beam loss in Interaction Regions

2.1. Collider IRs.

Fig. 1 shows a vertical schematic view of a complete IR [4]. SSC plans called for two detectors in the East IRs to operate at lower β* than those in the West cluster. The distance L* between the interaction point (IP) and the nearest quadrupole magnet QL1 ranges here from 20.5 m (baseline design) to 25 m (SDC detector) and 35 m (GEM detector). Fortunately, β* and the

peak luminosity $\mathcal{L}$ are weak functions of L* (see Table 1). So, SDC luminosity is only 9% lower than the baseline one. For GEM, losing 26% of the luminosity, one gains a spacious detector-free region, that simplifies access to the detector and allows for significant reduction of particle background. The design [4] is compatible with even larger L* - up to 90 m. For any given L*, the lowest β^* at collisions corresponds to β_{peak} = 9 km in the triplet, that makes it the smallest aperture in the machine. Fig. 2 is a schematic of the GEM detector and shielding configuration in the East IR experimental hall [5].

2.2. Beam Loss and Collimators.

There are a variety of reasons causing unintentional beam loss in the Collider. Besides a wide spectrum of cases during accelerator commissioning, the main two categories under normal operation are:

1) *Coherent Beam Motion* - multi-bunch instabilities, control problems and hardware errors during injection, ramping, collisions and beam abort, as well as a very unlikely accidental loss of a full beam (catastrophic accident).

2) *Incoherent Beam Motion* - transverse and longitudinal emittance growth due to single-bunch instabilities, power supply ripple, magnetic imperfections, elastic and diffractive protons from beam-gas, *pp*-collisions, and beam-scraper interactions.

In principle, beam loss of the first type can happen anywhere in the machine, while the second type occurs predominantly at the small apertures, e.g., in the low-β quadrupoles (LBQ). Beam loss results in deleterious effects in collider and detector components, ranging from mundane to rather dramatic [1, 6, 7]:

- Excessive particle background in detectors;
- Radiation impact on personnel and environment;
- Superconducting magnet quench;
- Additional heat load to cryogenics;
- Accumulation of radiation dose, shortening components lifetime;
- Overheating of critical components;
- Total destruction of some units via explosion.

A very reliable beam abort system is a first "must be" protective measure at superconducting accelerators. A multi-component beam collimation system has been proven necessary at the colliders [8, 9] to protect accelerator equipment against irradiation, to sustain favorable

background conditions in the detectors, to maintain operational reliability over the life of the machine, and to reduce the impact of radiation on personnel and the environment. Fig. 3 shows the locations of the collimators in the East IRs. The set consists of 10 collimators with movable jaws and 4 collimators with fixed aperture. Collimators of the first group intercept high energy protons (mainly diffractive) produced in beam interactions all around the machine and deal with both categories of beam loss introduced above. Detailed studies [9] show that the optimal jaw position is 16 to 20σ from the circulating beam axis. The collimators have a steel jaw 2.8-m long surrounded with steel shielding 0.35-m thick and 4.5-m long.

Fixed aperture collimators on either side of the interaction point (IP) just in front of the first LBQ are the main way to protect the final focus triplet from the intense radiation generated at the IP. Optimization studies [1, 10] show that a 3-m long steel collimator with a 25-mm diameter aperture is a good choice. Each collimator is made of stainless steel 300-400 mm in diameter, surrounded with 0.75-m thick steel shielding (groundwater protection) followed by about 1-m thick concrete shielding (Fig. 2). Shielding details are in section 6 below.

2.3. Source Term.

In the interaction regions at normal operation there are three major sources of radiation:

- Particle production at the interaction point in 20×20 TeV *pp*-collisions at 10^8 Hz rate ($\mathcal{L} = 10^{33}$ cm^2 s^{-1}).

- Interactions of beam with the residual gas in the beam pipe both in the warm ($\pm$ L*) and in the cold (> L*) sections. Based on a pressure of 10^{-8} torr of nitrogen in the warm regions of the beam pipe, and a baseline content of residual gas in the cold sections (H_2+CO+CO_2), corresponding beam loss rate is about 10^4 proton per meter per second from two beams.

- Quasi-local beam halo interactions with the beam pipe in the triplet. With the beam collimation system maximum loss rate of 5×10^4 proton per meter per second can occur at the β_{peak} location about 70 m from the IP and some higher rate on the collimators CLESIR and CLENIR [9] at about 180-m distance from the IP.

Studies show that the first source determines the radiation levels in the detector components [1, 5], in the final focus triplet [1, 10], and in the experimental hall [11]. The rest of the paper describes results of realistic Monte Carlo studies of radiation effects due to the above sources.

2.4. Simulations.

In this paper we assume standard parameters for the Collider: a luminosity 10^{33} cm^{-2} s^{-1} for 20 × 20 TeV *pp*-collisions, and 10^7 s detector operational year. 4000 to 10000 *pp*-events were generated with the DTUJET92 code and used as input in hadronic and electromagnetic shower simulations and subsequent low-energy neutron transport with the MARS12 code. Energy thresholds are 1 MeV for muons and charge hadrons, 0.1 MeV for electrons and photons, and 0.5 eV for neutrons. The last one (cadmium cut-off) is used instead of thermal energy ~ 0.01 eV, because of CPU saving and because neutrons with E<0.5 eV are easily eliminated from consideration assuming a small addition of boron in shielding concrete. Calculated values are 3-D distributions of energy deposition density, of charge and neutral hadron fluence (E > 14 MeV), of low-energy neutron fluence (0.5 eV < E < 14 MeV), of partial fluences of charge particles (hadrons and muons) and all neutrons, of star density (density of inelastic hadron interactions), as well as total energy deposited in each component. Power and accumulated dose in elements were derived from the energy deposition distributions. Residual dose rates were calculated using star density distribution, phenomenological radionuclide production model, and point-kernel shielding algorithm for the subsequent decay of radionuclides and photon transport through material.

All the details of 3-D geometry, materials and magnetic field maps in 50-mm aperture quadrupoles QL1, QL2 and QL3 (G = 191 T/m) with 42-mm ID and 44.6-mm OD beam pipe [10], in 85-mm aperture vertical bending magnets BV1c (B=6.4 T) with 78-mm ID and 83-mm OD beam pipe are included in the simulations extended through the cold mass, supports, cryostats to the tunnel concrete walls followed by 1 meter of rock (Austin chalk). For the purpose of this paper, the detailed description of detector geometry, materials and magnetic field is used for the first 2-m radial distance from the beam line, followed by a simplified description at larger distances. The detailed description of collimators and shielding as well as geometry and materials through the whole tunnel and experimental halls are included in the simulations.

3. Energy deposition in the low-β optics due to *pp*-collisions

3.1. Energy Balance in *pp*-Collisions and Studied Cases.

All general purpose collider detectors deal only with a minor portion of energy produced at the IP. Fig. 4 shows the fraction of the total energy emitted from the IP as a function of pseudorapidity [1, 5]. Only 0.5% of energy is deposited in the SDC and GEM central and endcap calorimeters, and 3-4% - in the forward calorimeter. The rest is deposited in the accelerator structures, which could result in undesirable consequences: quenching of superconducting

magnets, excessive heat load to the cryogenic system, radiation damage in magnet components, and increased residual activation dose rate. About 36% of the collision energy is absorbed in the first collimator and LBQ's and 15% in the BV1c-BV1 region. Roughly 23% of the collision energy is removed by diffractive and elastic protons and deposited over a long distance in the machine on the first or even following turns. About 22% of energy is carried by neutral particles in the straight ahead direction.

Four cases are considered in detail in this section for two values of L* and of the first collimator inner diameter ID:

a) L* = 20.5 m, ID = 25 mm;

b) L* = 20.5 m, ID = 42 mm;

c) L* = 20.5 m, ID = 42 mm, no magnetic field in the detector and in the LBQs;

d) L* = 35 m, ID = 42 mm.

Calculations for L* = 25 m are also performed and some results are presented here. Case (c) with no magnetic field is considered to show the effect of the field.

3-D distributions of energy deposition density and particle fluence in the final focus triplet components are scored during MARS12 running sessions. At the conclusion, a few values of a practical interest are calculated using those distributions. Results are presented in the subsections below for each of four L*/ID combinations (cases a, b, c, d).

3.2. Energy Deposition Rate.

The quench stability of a superconducting magnet depends on the space-time distribution of the deposited energy, the proximity of the operational point to the critical one, and on the details of the cryogenic cooling system. For a given magnet, low-β quadrupoles and vertical bending dipole in our case [10], power deposited per unit volume of superconducting coil is a measure of such a stability. Taking into account the Tevatron experience [12] and studies [6, 13], one can assume ε_q = 3 mW/g as the quench limit and hence the maximal energy deposition density in the coils of the SSC type final focus magnets.

Calculations [1, 6, 10, 13] show that there is a significant variation of energy deposition across the coils and along the magnets. Energy deposition is always peaked in the innermost region of the coil followed by a rapid decline with the radius. Even though the angular distribution of particles from the IP is azimuthally symmetrical, fields encountered in the magnets cause energy deposition and particle fluence to be concentrated either in horizontal or

vertical planes. Contrary to the arc magnets, where such an azimuthal variation is as high as a factor of 100 [6, 13], in the low-β quadrupoles maximal and minimal energy deposition densities along the ϕ-angle differ by about a factor of 3 to 4. Below results are presented for maximum values in the azimuthal distributions while focusing attention on longitudinal and radial behavior.

Fig. 5 shows energy deposition density rate at the innermost radius of the superconducting coils of the final focus magnets as a function of the path length from the IP for the baseline interaction rate of 10^8 int/s. As one could expect and as shown in earlier studies, the maximum energy deposition, ε_{max}, always occurs in the first LBQ. It is important to note that $\varepsilon_{max} << \varepsilon_q$ for all four cases considered, being less than 10% of the quench limit. ε_{max} scales almost linearly with luminosity and with beam energy, so for SSC at $\mathcal{L} = 10^{34}$ cm^2 s^{-1} $\varepsilon_{max} \approx \varepsilon_q$ and some additional measures are required to reduce ε_{max} .

Decreasing the collimator ID from 42 to 25 mm, one reduces ε_{max} by about 20%. Increasing the detector-free space L* from 20 to 35 m causes about the same reduction. Results for L* = 25 m are very close to those for L* = 20 m. In general, the energy deposition is lower for the distant components. But due to effect of the magnetic field on shower development, the energy deposition density, chosen as a maximum in the azimuthal distribution and with a collimator in front of the first LBQ, almost always reaches its maximum at the end of each low-β quadrupole with alternating polarity. The effect is clearly seen by comparing Figs. 5b and 5c: with the magnetic field switched off one has a linear decrease of ε_{max} with only minor peaks in the interconnect regions. This emphasizes the necessity of including the magnetic field in realistic considerations of the IRs.

Energy deposition beyond the last quadrupole, QL3, is significantly lower because the aperture jumps from 42 to 78 mm starting at the interconnect region between QL3 and BV1c. With equal apertures in the quadrupoles and the common vertical bending magnet, ε_{max} in the dipole is noticeably higher.

Lateral distributions of energy deposition density in the coils, collar, yoke, and cryostat up to the magnet outer wall are presented in Fig. 6 at the longitudinal peak location close to the far end of the first quadrupole QL1. For all realistic cases considered, there is a rapid drop across the coils and the collar - 100-fold gradient over the first 50 mm (≈ 3 radiation lengths, which is the proper yardstick in view of electromagnetic nature of the energy deposition in this region) - and then a much reduced slope with another factor of 10 decrease to the magnet wall. The hypothetical case with zero magnetic field (Fig. 6c) gives a wrong prediction just as in the

previous paragraph (Fig. 5c): a much steeper lateral gradient which is explained by compressed showers with much smaller angle particles, not influenced by the magnetic field. Other parameters - the collimator ID and distance L* - have only a minor effect on the radial distribution.

3.3. Heat Load To Cryogenics.

Even with a collimator installed upstream of QL1, total energy deposited in the low-β quadrupoles and especially in the first one is extremely high [1, 6]. Total heat Q to be removed from QL1 is about 50 Watts at baseline luminosity (compared to about 3 Watts at 4 K in the arc magnets), which presents the most severe design challenge [10]. Fig. 7 shows the longitudinal distribution of heat load to the triplet cold mass. In its main features the behavior of total energy deposited follows that of the ε_{max} -distribution. About 50% of the total power in the triplet is deposited in QL1, i. e., 28.57, 48.50, and 40.07 Watts for cases (a), (b) and (d), respectively. One can see, that the effect of collimator aperture is quite significant: decreasing the aperture from 42 to 25 mm reduces Q in the first quadrupole by 40%. Further ID reduction to 20, 15 or 10 mm gives even higher reduction, but it becomes unacceptable from the viewpoints of accelerator design [10] and albedo particle background to detectors [1] (see also subsection 4.1 below). Increasing the detector-free space L* from 20 to 35 m results in 20% reduction of heat load in QL1. Data for L* = 25 m are very close to those for L* = 20 m. It is interesting that power deposited in the other elements QL2, QL3 and BV1 is the same in each of the realistic cases considered. Case (c), with no magnetic field, again gives rather different results.

One sees that with the appropriate choice of the collimator and with LBQs cooled by superfluid Helium (He II) one can build these high-gradient magnets compatible with the baseline luminosity. The recommended design parameters [10] are: four 88-mm cooling channels in yoke, liquid supply line routed outside of the cold mass, 78-mm diameter corrugated cooling ducts, two heat exchangers for baseline heat load. Results on heat load scale linearly with the luminosity, becoming 10 times higher at $\mathcal{L} = 10^{34}\ \mathrm{cm^2\ s^{-1}}$. The design [10] is upgradable with addition of a beam cooling insert and two additional heat exchangers.

3.4. Accumulated Dose.

Dose accumulated in the accelerator and detector components results in degradation of their properties through radiation damage and shortens their lifetime in some cases to well below the design lifetime of 25 years for the whole complex. For the "hottest" regions, the measure is again maximum energy deposition density integrated over some period, e.g., 1 year. The period depends, of course, on the operational scenario. Assuming 10^7 s as a detector operational year at

baseline luminosity (10^{15} int/yr), results of section 3.2 are rescaled to permit analysis, related to material specifications and expected accelerator component lifetimes in the IR region.

Figs. 8 and 9 show the longitudinal and lateral distributions of maximum annual dose in the low-β quadrupoles and dipole BV1c for cases (a) through (d). All conclusions of section 3.2 on various dependencies apply equally to these problems. The peak dose in QL1 is 200 to 250 Mrad/yr. Peak annual dose in QL3 and in the first section of QL2 is about 75 Mrad, in the second section of QL2 it is 125-150 Mrad, and in the dipole BV1c it is less than 25 Mrad. The dose is much lower in the outer coil and in the cryostat.

The above numbers are the basis for the choice of the materials to be used in the magnets. The SSC plan called for 1000 Mrad as a radiation damage limit for materials in the arc magnets. Thus QL1 coils will survive only for 4 to 5 years at baseline luminosity and 10 times less duration at $\mathcal{L} = 10^{34}\,cm^2\,s^{-1}$. The other elements will last longer. One obvious way to increase the lifetime is to use more radiation resistant materials in the low-β quadrupoles coils. For kapton and polymide, e.g., the limit is about 5000 Mrad. With an optimal collimator in front of QL1, further dose reduction may be achieved by a beam cooling insert. It is found [10] that with about 7 mm stainless steel insert between beam pipe and (enlarged) coil aperture, one can reduce a peak energy deposition by a factor of 2 to 4. The effect is even higher with the insert made of heavier materials like tungsten.

3.5. Particle Fluence.

As stated above, in magnet regions close to the beam, where electromagnetic showers from π^0's created at the IP and by hadron interactions with the beam pipe in the final focus triplet are dominant, the energy deposition determines all aspects of short and long term component stability. At larger radii other mechanisms become important. In some applications - radiation damage to electronics, detectors response, radionuclide production, radiation in access shafts and labyrinths - often particle (neutron) fluence is a more important measure. In this subsection results are presented for hadron and low-energy neutron distributions in the low-β magnets, which can be used for analysis and as a source for a subsequent transport in the tunnel and experimental halls. Results for all four standard cases are integrated over a detector operational year.

Fig. 10 shows the longitudinal distribution of charged and neutral hadron fluence Φ_h (E > 14 MeV) in the magnet cryostat. Results for neutrons with lower energy Φ_n (0.5 eV < E < 14 MeV) are presented in Fig. 11. In general, the shape of the distributions resembles the ones for energy

deposition with magnetic field induced peaks at roughly the same locations. There is one interesting difference in the collimator effect: a smaller collimator aperture better protects the entrance to the triplet and distant magnets, but enhances fluence at the downstream end of QL1 due to increased number of interactions of hadrons from the IP with the beam-side collimator surface, which generate numerous lower energy hadrons which are then deflected by the QL1 magnetic field.

Radial distributions of particle fluence in the first quadrupole at the longitudinal peak are shown in Fig. 12. One should note the following:

- the distributions are much flatter compared to the energy deposition ones, especially for low-energy neutrons;
- low-energy neutron fluence Φ_n, being lower than Φ_h at the innermost radius, then becomes higher and through the build-up region exceeds the hadron fluence at the outer cryostat wall by about a factor of 10;
- there is only a minor dependence of Φ_n and Φ_h radial distributions on distance L* and the collimator ID;
- the effect of the magnetic field on the shape of radial distributions is almost negligible, but the absolute value of particle fluence in the magnets and that leaking out of the outer surface is underestimated by a factor of 3, if fluence is calculated without magnetic field.

Annual particle fluence in the magnets is very high: in the superconducting coils of QL1 it is up to 10^{15} cm^{-2} yr^{-1}, and in the cryostat it is close to 10^{13} cm^{-2} yr^{-1} for hadrons and to 10^{14} cm^{-2} yr^{-1} for low-energy neutrons. In QL2 and QL3 these values are about 3 times lower at maximum, and in BV1c maximum fluences are about 10% of those in QL1.

3.6. Residual Dose Rate.

Gamma dose rate due to residual radioactivity in detector and accelerator components is of concern to personnel during maintenance periods. The maximum dose rate on contact in the near-beam region can be as high as 5 rem/h for the forward calorimeter and 50 rem/h for the collimator [1, 5]. Dose is significantly lower for larger radii, say on the outer surfaces of the components.

Fig. 13 shows the calculated residual dose rates in the low-β magnets. The quasi-saturation regime has been considered with 10^7 s irradiation time and zero cooling time. The longitudinal distributions of contact dose rate presented were averaged transversely over the cryostat ($15 < r < 35$ cm) and over the ends (flanges) of the components ($2.5 < r < 37$ cm). One can see that the

contact dose rate right after shutdown is rather high, on a few hundred mrem/h level. These values scale inversely with distance from the component. Due to decay of short-lived isotopes dose rate drops by a factor of two within a day after shutdown and continues to decrease with further cooling (Fig. 14). To reduce the residual dose rate further, it is good practice to use low-activated materials (lower atomic number in general) in all the critical regions. With appropriate precautions - some cooling time (a day or so), fast connects, extended tools, and local mobile shielding in some areas - the residual radioactivation concerns of the IR components can be overcome. Only in a few cases may remote control be required.

4. Particle background in detectors

Over last two years a few groups have performed comprehensive studies on neutron and photon backgrounds due to *pp*-collisions in the SSC and LHC detectors. As a result, sophisticated shielding configurations (flared beam pipe, albedo traps, shielding in the forward region and inside detectors, using materials like borated polyethylene, barite concrete and graphite) were found which ensure that the detectors will operate at the baseline luminosities (see, e.g., [5]). In this section results on particle backgrounds, induced by 20×20 TeV *pp*-collisions, by beam-gas interactions, and by local beam loss in the final focus triplet are compared.

4.1. *pp*-Collisions.

Results calculated with MARS12 of neutron, charged hadron and muon fluxes in a few longitudinal and radial regions of the GEM detector (Fig. 2) are presented in Table 2 (see columns 3 to 5 for *pp*-induced background). Charged particle flux, dominating at the beam pipe, rapidly drops with radius, and neutron flux (accompanied by photons) dominates through the whole detector body. Of course, to see the effect in different detector elements (central trackers, calorimeters, muon chambers), the fluxes should be weighted with individual response functions for different particle types. But overall charged particles originating from *pp*-collisions play the main role at small radii and neutrons (and photons) are responsible for radiation effects at $r > 1$m.

Particle backgrounds in the detector, produced by hadronic showers in the collimator in front of the first LBQ are a weak function of collimator location in the 20 to 35-m range, assuming the same shielding between detector and collimator. But with the collimator farther from detector, there are many possibilities to protect the detector from radiation, generated in the collimator and low-β quadrupoles [5]. The smaller the collimator aperture, the higher the fluence of particles scattered back to detector: neutron albedo for collimator ID = 25 mm is 2 to 2.5 times higher than

that for ID = 42 mm [1]. Particle leakage from collimator and magnet outer surfaces is also higher for smaller collimator ID (see subsection 3.5) and it is found that ID = 25 mm compromises machine and detector requirements.

4.2. Beam-Gas.

Particle fluence due to interactions of 20 TeV beam with nuclei of residual gas is calculated assuming a gas pressure and content in the warm and cold sections of the IR beam pipe as indicated in section 2.3. Results are presented in Figs. 15-18 for the GEM geometry (Fig. 2) with $L^* = 35$ m. Charged hadron and neutron fluences are given in the detector central region ($\pm$ 2 m) and in the forward muon spectrometer (19 m from the IP) for three radial intervals. For the given optical and collimation schemes there is almost no contribution to these regions from beam-gas interactions outside the final focus triplet. Numerical results given in Table 2 (columns 6 to 8) are collected from interactions of beam protons with residual gas in $\pm$ 120 m region from the IP. Figs. 15-18 show the ratios of particle fluence, produced over the length L from the IP, to that for L = 120 m. Details of detector, shielding, lattice and experimental hall/tunnel interface all contribute to the behavior of curves on those figures: sharp increases - especially for low-energy neutrons - at $L = L^* = 35$ m and at L = 50 m (hall to tunnel transition).

At baseline luminosity and at design residual gas pressure in the IRs, the contribution from beam-gas interactions to the background in different parts of the collider detectors is less than a few percent (see Table 2). But this contribution becomes significant if the attainable vacuum in the detector region is worse than the assumed 10^{-8} torr and/or luminosity is lower than the baseline one with the same beam intensity (1.3×10^{14} ppp in the SSC). The last can easily happen during first years of operation, so special precautions are required to mitigate the above problem.

4.3. Beam Halo in the Triplet.

As mentioned above, $\beta^* = 0.5$ m at collisions corresponds to $\beta_{peak} = 9$ km in the low-β quadrupoles. For 50-mm bore quadrupoles with 42-mm ID beam pipe, the corresponding physical aperture is 27σ at the collisions and 17σ at injection. This makes the triplet a bottleneck for halo particles, so even with collimators in the machine, the LBQ will experience increased beam loss, being a source of detector background. The estimated theoretical maximum is about 10^7 Hz beam loss rate at these locations. With collimators in the collider at 16-20σ distance from the beam axis, maximum beam loss rate is reduced to 5×10^4 protons per meter per second [9].

Fig. 19 shows annual low-energy neutron fluence at a radial distance 1.5-2 m from the beam axis, caused by quasi-local beam loss at β_{peak} region compared to that due to beam-gas

interactions. Results are presented for L* = 20.5 m with no shielding around LBQs. Hadrons with E > 14 MeV contribute less than 10% to the total particle fluence. There is a large increase of neutron fluence in the tunnel that starts 55 m from the IP due to reflections from the walls for both sources and a proximity to the beam loss at QL3. Near the detector the fluence caused by beam loss at the β_{peak} location is lower compared to that from other sources. The last column of Table 2 shows muon flux in the GEM detector (Fig. 2), generated in the 20 TeV proton beam interactions with the collimators CLESIR and CLENIR at 182-m distance from the IP. This source contributes less than 10-20% of the total muon flux in the detector. Contribution from this source to neutron and charge hadron flux in the detector is negligible.

5. Neutrals and long range beam loss

About 22% of the energy in 20 × 20 TeV *pp*-collisions is carried by neutrals in the forward direction through the final focus triplet. Fig. 20 shows the photon and neutral hadron spectra downstream of the vertical bending dipole BV1c [1]. The spectra are very energetic with mean energy 1.1 TeV for photons and 3.5 TeV for neutral hadrons (mainly neutrons). This neutral beam may be useful for luminosity monitoring or other purpose. Absorbers appropriate to contain the energy deposited by the neutral beam can be combined with pairs of collimators (CLESIR, CVESIR) and (CLENIR, CVENIR) at 182-m distance on each side of the IP [1]. Compact steel absorbers - about 1.5 m long and 0.2-0.3 m diameter (Figs. 21 and 22) - surrounded by a shield in common with that of the collimators are sufficient to act as an effective neutral beam dump. Neutral beam spot size is large enough, so there is no problem with local energy deposition effects. The 70 Watts of power generated at baseline luminosity may be removed with a simple cooling system.

About the same amount of the collision energy - 23% - is carried out by diffractive and elastic protons, that contribute to beam loss over long distances in the collider. Maximum loss rate due to this source can be as high as 2×10^5 protons per meter per second at some superconducting magnets, which is much too high. The collimation system [9] also solves this problem: with collimators CVENIR and CVESIR downstream of the vertical dipoles BV1c, the peak loss rate on superconducting elements caused by that high-energy component of the IP radiation is reduced to 6×10^3 protons per meter per second. Calculated in [9] beam loss rates at the collider IR collimators are shown in Fig. 23.

6. Radiation shielding in the IRs

As indicated in subsection 2.2, the IR collimators are surrounded with appropriate shielding to meet groundwater activation criteria. In the experimental halls each fixed aperture collimator is surrounded with 0.75-m thick steel shielding followed by about 1-m thick concrete (Fig. 2). This concrete shielding is extended from the forward calorimeter to the first LBQ and protects detector against low-energy neutrons. From a radiation point of view there is no need for any shielding around the low-β quadrupoles. However, shielding might be installed around the quadrupoles at 1.2-m distance from the beam axis to bring the background particle fluxes at the detector down to the tolerable levels [5]. For an upgrade luminosity of $\mathcal{L} = 10^{34}$ c m^2 s^{-1}, additional protection of both groundwater and detector must be provided: collimator shielding must be increased transversely by 0.4 m of steel, and shielding is absolutely required for the accelerator components with 1.2 m of concrete around the quadrupoles in the experimental hall, and 0.6 m of concrete around the rest of the final focus triplet in the tunnel. This shielding might be even thicker depending on the tolerable background particle fluxes at the detectors.

The study of general radiation shielding in the SSC experimental halls was performed in [11]. It is shown, that the general purpose detectors, SDC and GEM, are well selfshielded and the radiation environment in the halls is determined by detector/accelerator interface zone. Calculated with several different methods, the roof shield thickness to achieve "open" status for the area is 6 m of concrete equivalent (ρ = 2.4 g/cm^3). The configurations of the SDC and GEM access shafts were also calculated, treating the shaft openings at ground level in the head-houses as "controlled" areas.

7. Conclusions

Results presented ensure that the chosen IR scheme is compatible with baseline parameters of multi-Tev high luminosity hadron colliders from both accelerator and detector viewponts, and can be a basis for further analysis and design work.

Acknowledgments

The author wishes to thank A. Drozhdin, G. Gilchriese, D. Groom, M. Harrison, R. Little, R. Stiening, and A. Van Ginneken for valuable discussions.

References

1. N. Mokhov, "Accelerator/Experiment Interface Issues at the SSC', Bulletin of the American Physical Society, Vol. **38**, No. 2, p. 908 (1993).
2. F. Bopp, R. Engel, D. Petermann, J. Ranft and S. Roestler, "DTUJET92", UL-HEP-93-02, Leipzig (1993).
3. N. Mokhov, "MARS12 Code System", Proc. SARE Workshop, Santa Fe (1993); N. Mokhov, "MARS10 Code System User's Guide", Fermilab FN-509 (1989).
4. Y. Nosochkov, E. Courant, A. Garren, D. Ritson, T. Sen and R. Stiening, "Current Design of the SSC Interaction Regions", SSL-Preprint-368 (1993).
5. M. Diwan, Y. Fisyak, N. Mokhov, D. Lee, L. Waters, Y. Efremenko, B. Moore, M. Marx, C. Wuest, J. Rutherfoord and V. Morgunov, "Radiation Environment and Shielding for the GEM Experiment at the SSC", SSCL-SR-1223 (1993).
6. I. Baishev, A. Drozhdin and N. Mokhov, "Beam Loss and Radiation Effects in the SSC Lattice Elements", SSCL-306 (1990).
7. D. Wilson, C. Wingate, J. Goldstein, R. Godwin and N. Mokhov, "Hydrodynamic Calculations of 20 TeV Beam Interactions with the SSC Beam Dump", Proc. of IEEE Particle Accelerator Conference, p. 3090 (1993).
8. M. Maslov, N. Mokhov and I. Yazynin, "The SSC Beam Scraper System", SSCL-484 (1991).
9. A. Drozhdin, N. Mokhov, R. Soundranayagam and J. Tompkins, "Toward Design of the Collider Beam Collimation System", SSCL-Preprint-555 (1994).
10. N. Mokhov, R. Schermer and R. Stiening, "The SSC Low Beta Quads Design Study", SSC Memo, June 4 (1991). D. Baritchi, C. Corbett, A. Jalloh, N. Mokhov, R. Schermer, and R.Stiening, "Conceptual Design Studies for a He-II Cooled Low Beta Quad IR Magnets", SSCL-Preprint-285 (1993); Presented at 5th IISSC Symposium, San Francisco (1993).
11. J. Bull, J. Coyne, N. Mokhov and G. Stapleton, "Shielding Consideration for the SSCL Experimental Halls", SSCL-Preprint-558 (1994); Presented at the 8th Int. Conference on Radiation Shielding, Arlington, TX (1994).
12. R. Dixon, N. Mokhov and A. Van Ginneken, "Beam-Induced Quench Study of Tevatron Dipoles", Fermilab FN-327 (1980).
13. N. Mokhov, Sov. J. Tech. Fiz., Vol. **24**, 694 (1979). M. Maslov and N. Mokhov, Particle Accelerators, Vol. **11**, 91 (1980). M. Maslov and N. Mokhov, in Proc. III ICFA Workshop, Protvino, p. 3 (1981).

Table 1. β-function and luminosity $\mathcal{L}$ at the SSC interaction point for different detector free spaces L^*.

L^* (m)	β^* (m)	$\mathcal{L}$(cm^{-2} s^{-1})
20.5	0.50	1.00×10^{33}
25	0.55	0.91×10^{33}
35	0.68	0.74×10^{33}
50	0.94	0.53×10^{33}

Table 2. Flux of neutrons (E>0.5 eV), charged hadrons (E>1 MeV) and muons (E>1 MeV) (particles/cm^2 /s) in a few regions of GEM detector due to 3 sources

z (m)	r (cm)	*pp*-collis			Beam-gas			Local
		n	**h**	μ	**n**	**h**	μ	μ
0-2	4-4.15	2.6×10^{6}	7.7×10^{6}	1.7×10^{4}	1.0×10^{4}	7.6×10^{4}	9.0×10^{0}	2.7×10^{-1}
	12-50	5.9×10^{6}	1.8×10^{5}	6.2×10^{2}	9.8×10^{3}	4.1×10^{2}	8.0×10^{0}	2.2×10^{-1}
	50-100	6.6×10^{6}	2.8×10^{4}	4.5×10^{1}	6.6×10^{3}	2.7×10^{1}	2.2×10^{0}	2.3×10^{-1}
	600-800	2.3×10^{3}	2.0×10^{-3}	4.2×10^{-3}	5.0×10^{1}	3.6×10^{-2}	6.7×10^{-1}	7.5×10^{-2}
7-10	30-60	1.4×10^{6}	2.9×10^{4}	7.9×10^{2}	5.8×10^{4}	4.6×10^{2}	1.3×10^{1}	4.0×10^{-1}
	125-200	1.8×10^{4}	7.8×10^{1}	4.8×10^{0}	4.2×10^{2}	1.1×10^{-1}	8.7×10^{-1}	3.0×10^{-1}
	600-800	9.1×10^{3}	3.3×10^{-1}	1.0×10^{-1}	2.2×10^{2}	8.4×10^{-2}	3.7×10^{-1}	3.1×10^{-2}
18-20	30-130	2.5×10^{4}	2.1×10^{3}	1.7×10^{2}	5.8×10^{2}	2.9×10^{1}	1.8×10^{0}	3.2×10^{-1}
	250-300	5.8×10^{3}	2.7×10^{0}	1.3×10^{0}	1.0×10^{2}	4.6×10^{-1}	1.3×10^{0}	5.0×10^{-1}
	600-800	2.5×10^{3}	1.3×10^{0}	4.1×10^{-1}	7.5×10^{1}	1.1×10^{-1}	8.2×10^{-2}	7.1×10^{-3}

FIGURE CAPTIONS

Fig. 1. Vertical view of an IR [4].

Fig. 2. GEM detector and shielding configuration [5].

Fig. 3. Collimator locations in the East Interaction Regions [9].

Fig. 4. Fraction of the total energy from the IP emitted as a function of pseudorapidity.

Fig. 5. Longitudinal distribution of maximum energy deposition at the innermost radius of the coils. Maximum values in the azimuthal distribution are presented. (a,b,c,d)

Fig. 6. Radial distribution of energy deposition at the longitudinal peak in QL1 (a,b,c,d).

Fig. 7. Longitudinal distribution of heat load to the triplet cold mass (a,b,c,d).

Fig. 8. Longitudinal distribution of maximum annual dose at the innermost radius of the coils. Maximum values in the azimuthal distribution are presented. (a,b,c,d)

Fig. 9. Radial distribution of annual dose at the longitudinal peak in QL1 (a,b,c,d).

Fig. 10. Longitudinal distribution of annual hadron fluence in the LBQ cryostat (a,b,c,d).

Fig. 11. Longitudinal distribution of annual low-energy neutron fluence in the LBQ cryostat (a,b,c,d).

Fig. 12. Radial distribution of annual particle fluence at the longitudinal peak in QL1 (a,b,c,d).

Fig. 13. Residual dose rate in the magnets on contact in a saturation immediately after shutdown.

Fig. 14. Time dependence of the residual dose rate.

Fig. 15. Charge hadron flux ($E > 1$ MeV) in the GEM detector central region, produced in beam-gas interactions over length L.

Fig. 16. Neutron flux ($E > 0.5$ eV) in the GEM detector central region, produced in beam-gas interactions over length L.

Fig. 17. Charge hadron flux ($E > 1$ MeV) in the GEM detector forward muon spetrometer, produced in beam-gas interactions over length L.

Fig. 18. Neutron flux ($E > 0.5$ eV) in the GEM detector forward muon spetrometer, produced in beam-gas interactions over length L.

Fig. 19. Annual neutron fluence (0.5 eV $< E <$ 14 MeV) at 1.5-2 m distance from the beam axis as a function of the path length from the interaction point due to beam-gas interactions and local beam loss in QL3 quadrupole.

Fig. 20. Neutron and Photon Spectra Downstream of the IP in the Straight Forward Direction.

Fig. 21. Energy Absorbed in 20-cm Radius Neutral Beam Dump as a Function of its thickness.

Fig. 22. Energy Absorbed in 2-m Thick Neutral Beam Dump as a Function of its transverse size.

Fig. 23. Beam loss rate at the IR collimators.

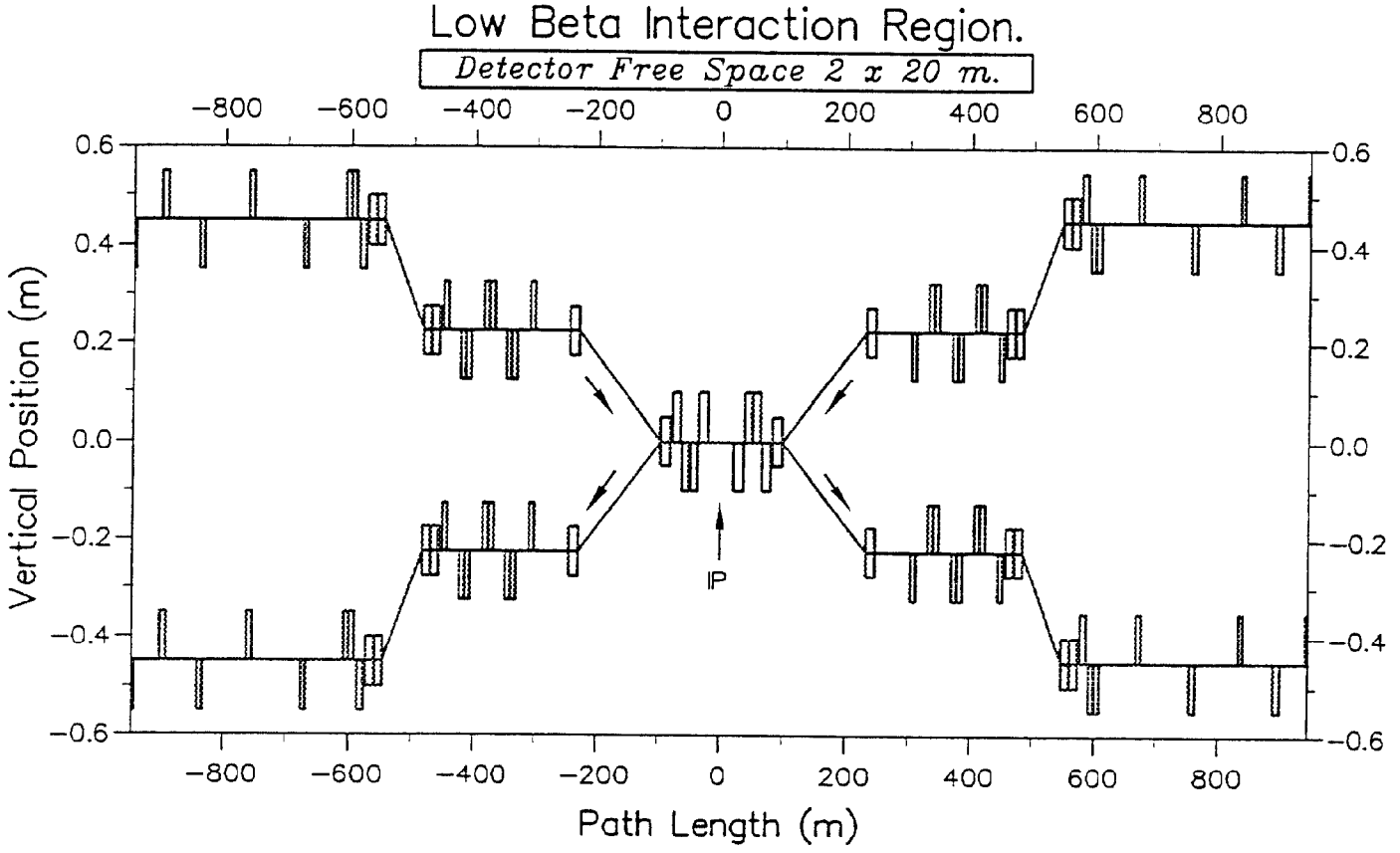
Low Beta Interaction Region.
Detector Free Space 2 x 20 m.
Vertical Position (m)
Path Length (m)
IP
−800
−600
−400
−200
0
200
400
600
800
0.6
0.4
0.2
0.0
−0.2
−0.4
−0.6

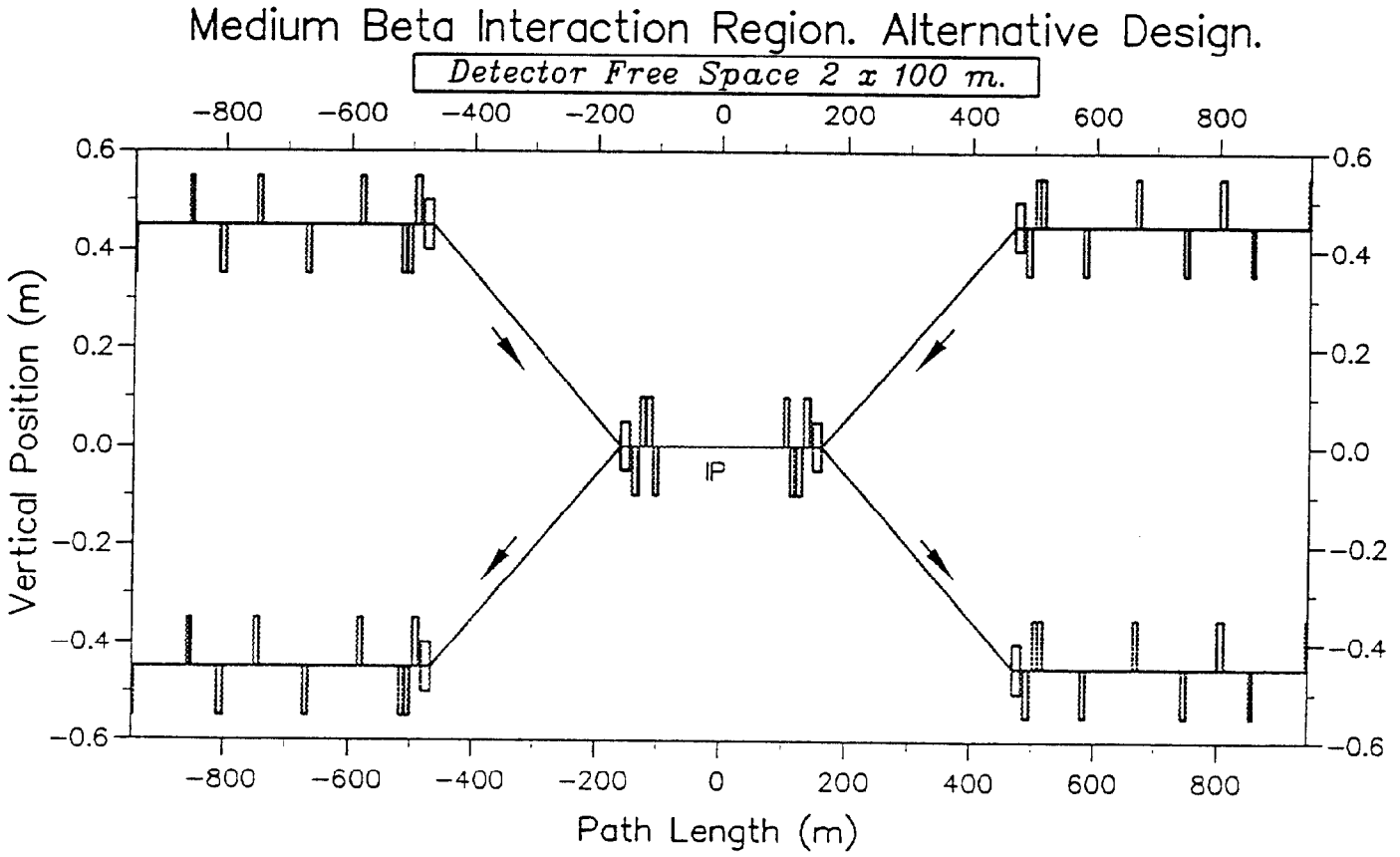
Medium Beta Interaction Region. Alternative Design.
Detector Free Space 2 x 100 m.
Vertical Position (m)
Path Length (m)
IP
−800
−600
−400
−200
0
200
400
600
800
0.6
0.4
0.2
0.0
−0.2
−0.4
−0.6

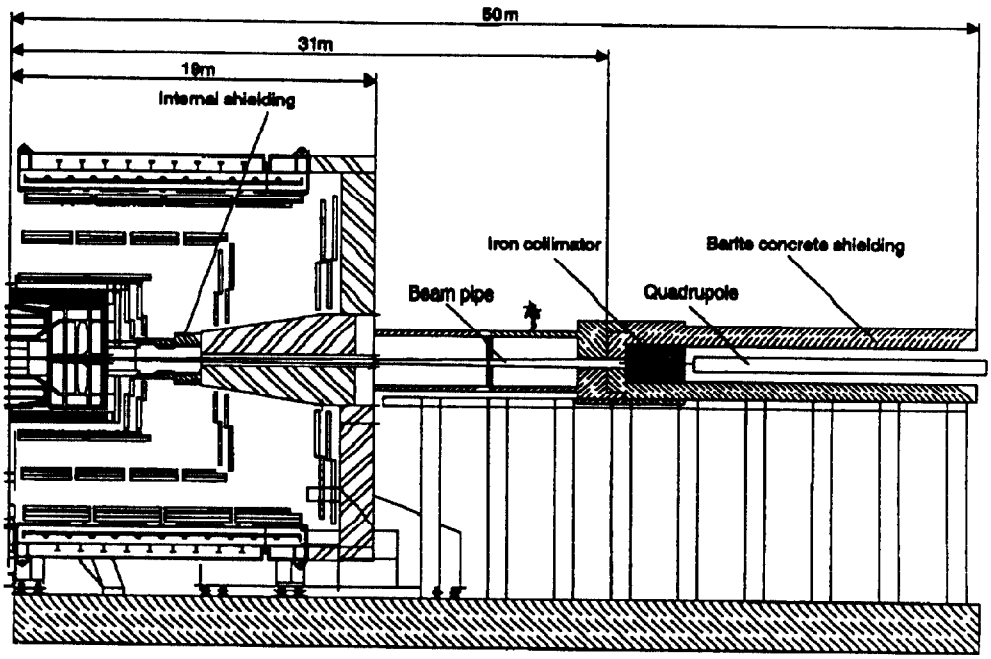
50m
31m
19m
Internal shielding
Iron collimator
Barite concrete shielding
Beam pipe
Quadrupole

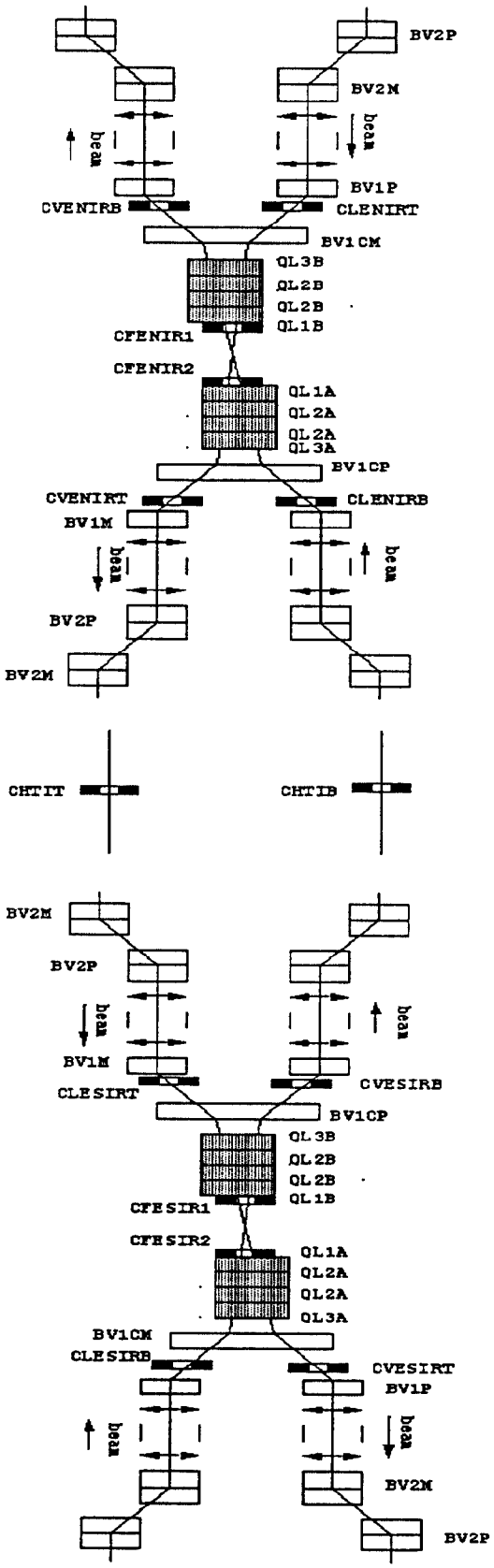
BV2P
BV2M
beam
beam
BV1P
CVENIRB
CLENIRT
BV1CM
QL3B
QL2B
QL2B
QL1B
CFENIR1
CFENIR2
QL1A
QL2A
QL2A
QL3A
BV1CP
CVENIRT
CLENIRB
BV1M
beam
beam
BV2P
BV2M
CHTIT
CHTIB
BV2M
BV2P
beam
beam
BV1M
CLESIRT
CVESIRB
BV1CP
QL3B
QL2B
QL2B
QL1B
CFESIR1
CFESIR2
QL1A
QL2A
QL2A
QL3A
BV1CM
CLESIRB
CVESIRT
BV1P
beam
beam
BV2M
BV2P

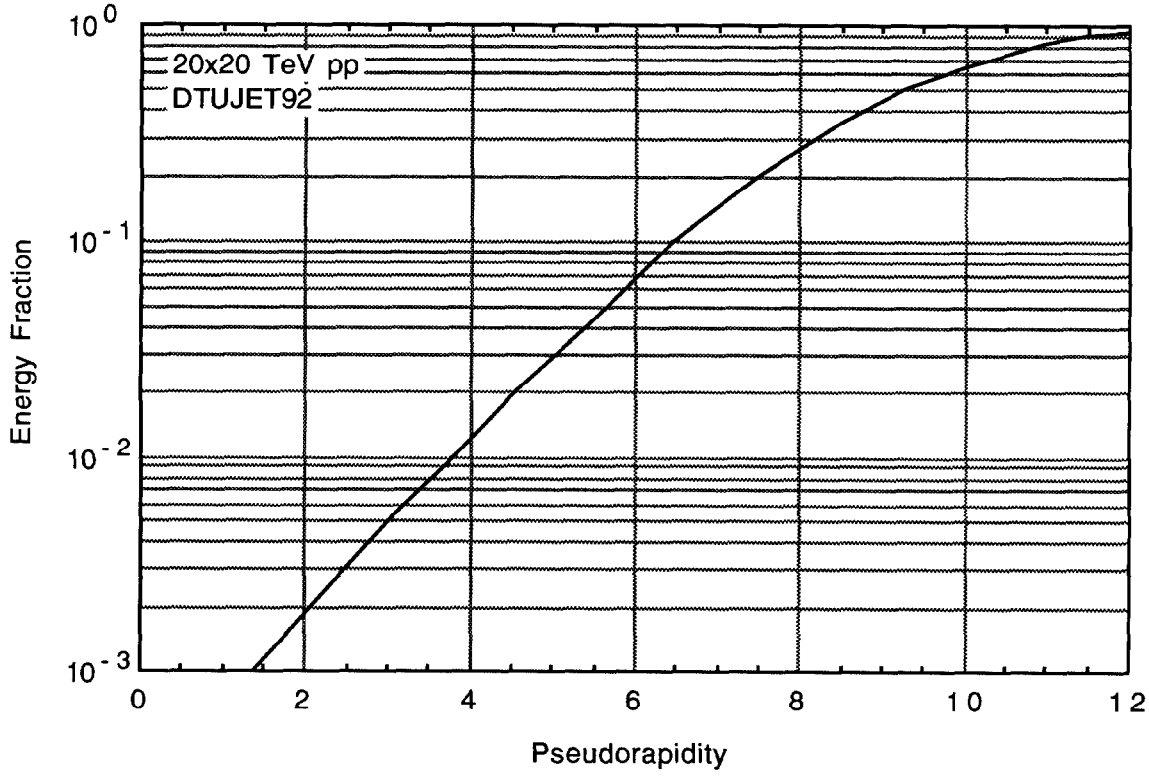
20x20 TeV pp
DTUJET92
Energy Fraction
Pseudorapidity
10^0
10^-1
10^-2
10^-3
0
2
4
6
8
10
12

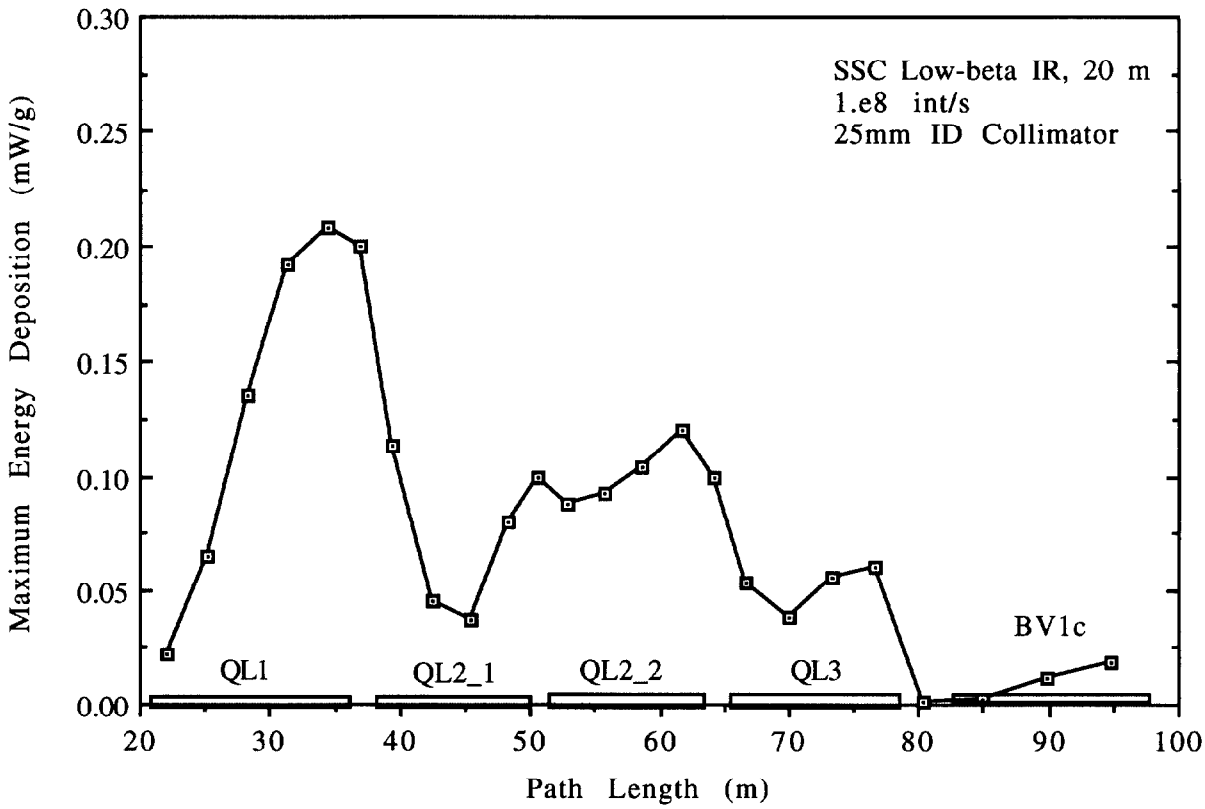
SSC Low-beta IR, 20 m
1.e8 int/s
25mm ID Collimator
Maximum Energy Deposition (mW/g)
0.30
0.25
0.20
0.15
0.10
0.05
0.00
QL1
QL2_1
QL2_2
QL3
BV1c
20
30
40
50
60
70
80
90
100
Path Length (m)

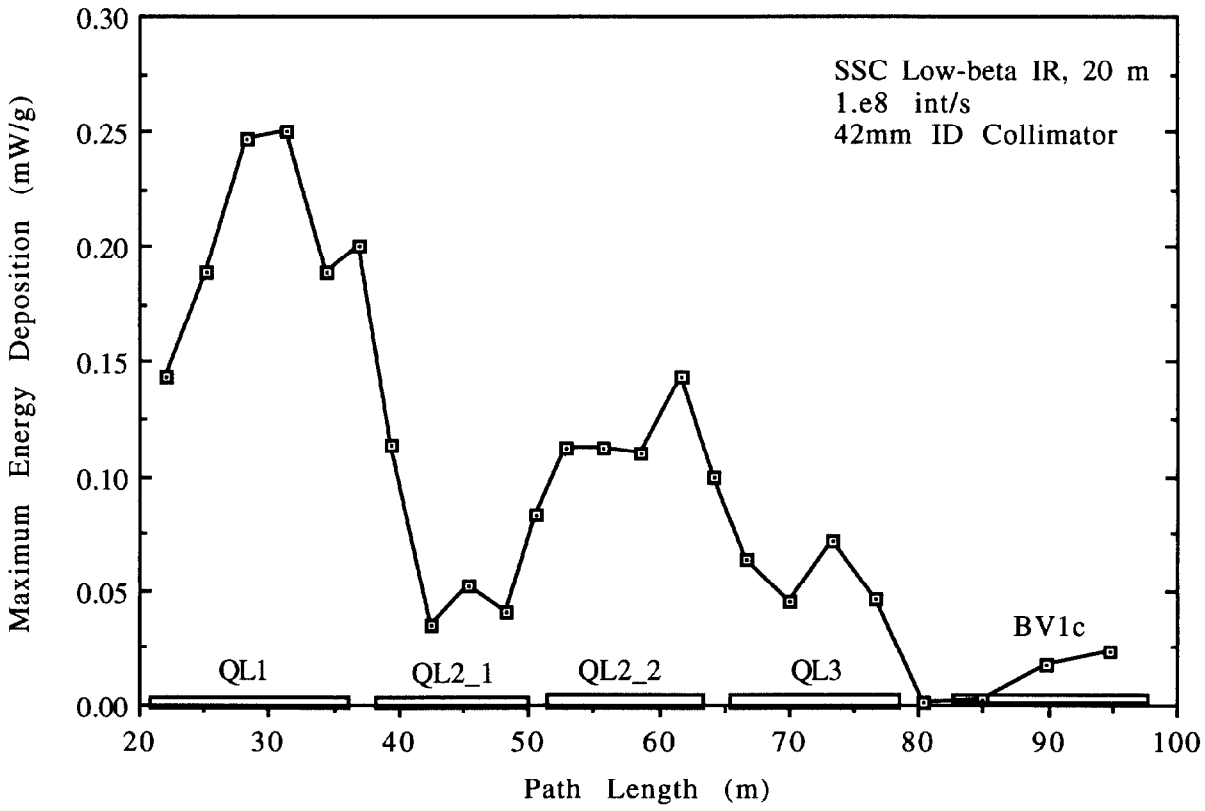
SSC Low-beta IR, 20 m
1.e8 int/s
42mm ID Collimator
Maximum Energy Deposition (mW/g)
0.30
0.25
0.20
0.15
0.10
0.05
0.00
QL1
QL2_1
QL2_2
QL3
BV1c
20
30
40
50
60
70
80
90
100
Path Length (m)

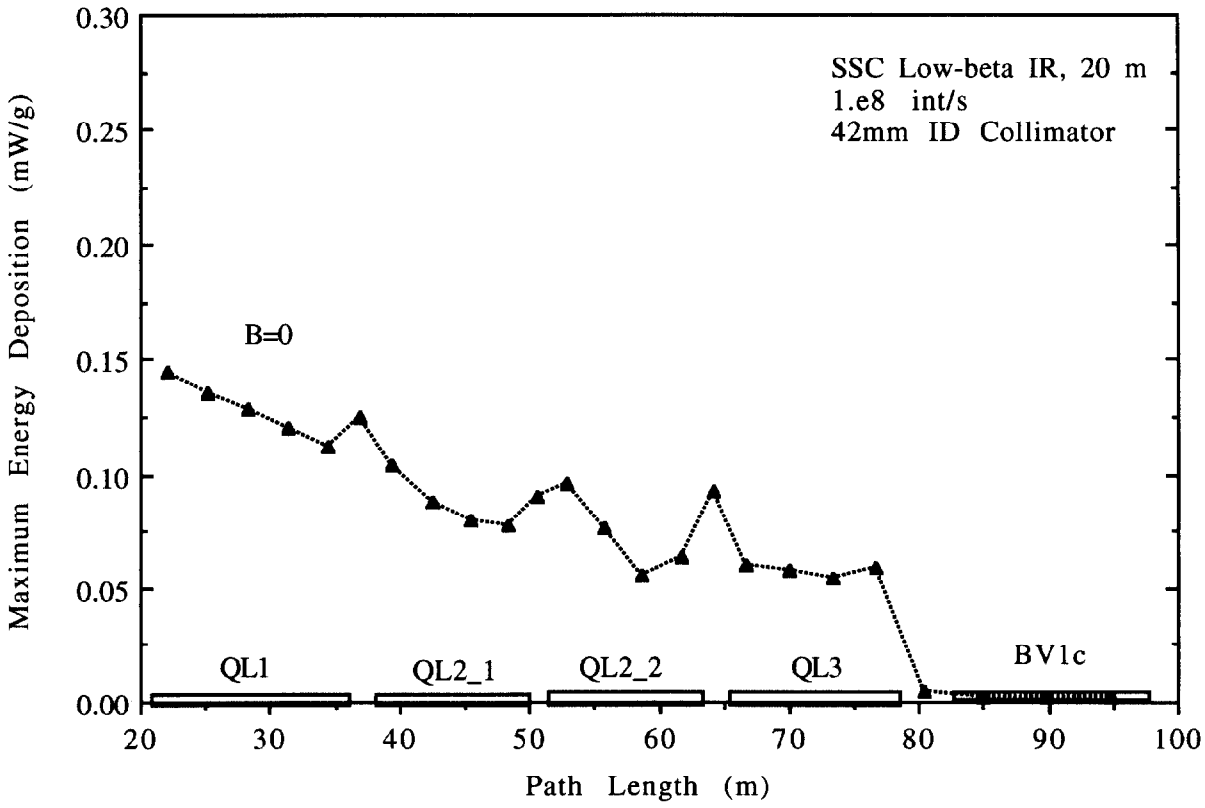
SSC Low-beta IR, 20 m
1.e8 int/s
42mm ID Collimator
B=0
QL1
QL2_1
QL2_2
QL3
BV1c
Maximum Energy Deposition (mW/g)
Path Length (m)
0.30
0.25
0.20
0.15
0.10
0.05
0.00
20
30
40
50
60
70
80
90
100

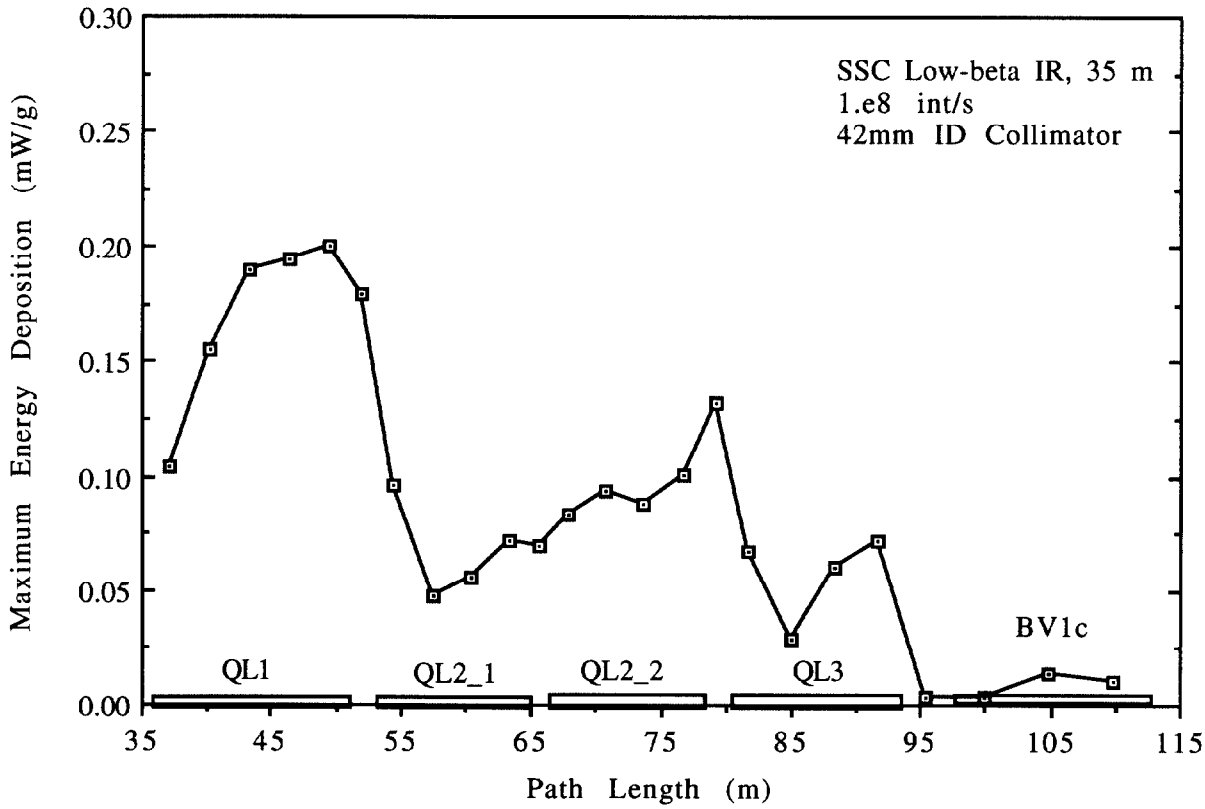
SSC Low-beta IR, 35 m
1.e8 int/s
42mm ID Collimator
Maximum Energy Deposition (mW/g)
0.30
0.25
0.20
0.15
0.10
0.05
0.00
QL1
QL2_1
QL2_2
QL3
BV1c
35
45
55
65
75
85
95
105
115
Path Length (m)

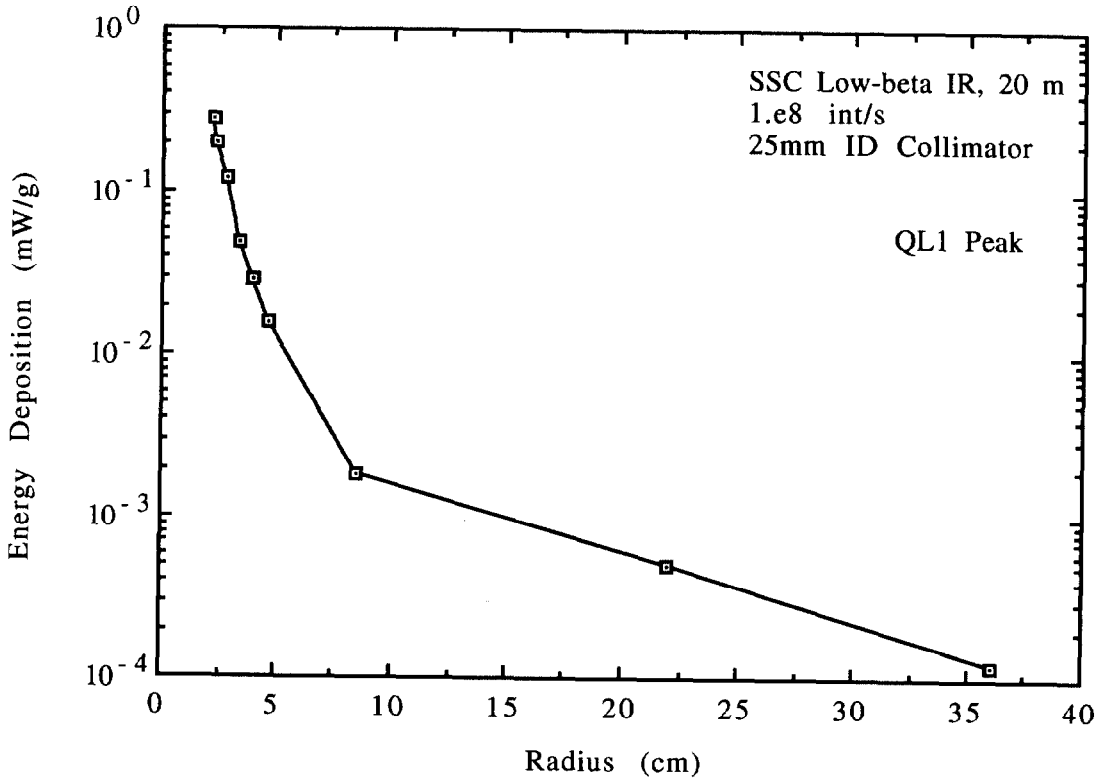
SSC Low-beta IR, 20 m
1.e8 int/s
25mm ID Collimator
QL1 Peak
Energy Deposition (mW/g)
Radius (cm)
10^0
10^-1
10^-2
10^-3
10^-4
0
5
10
15
20
25
30
35
40

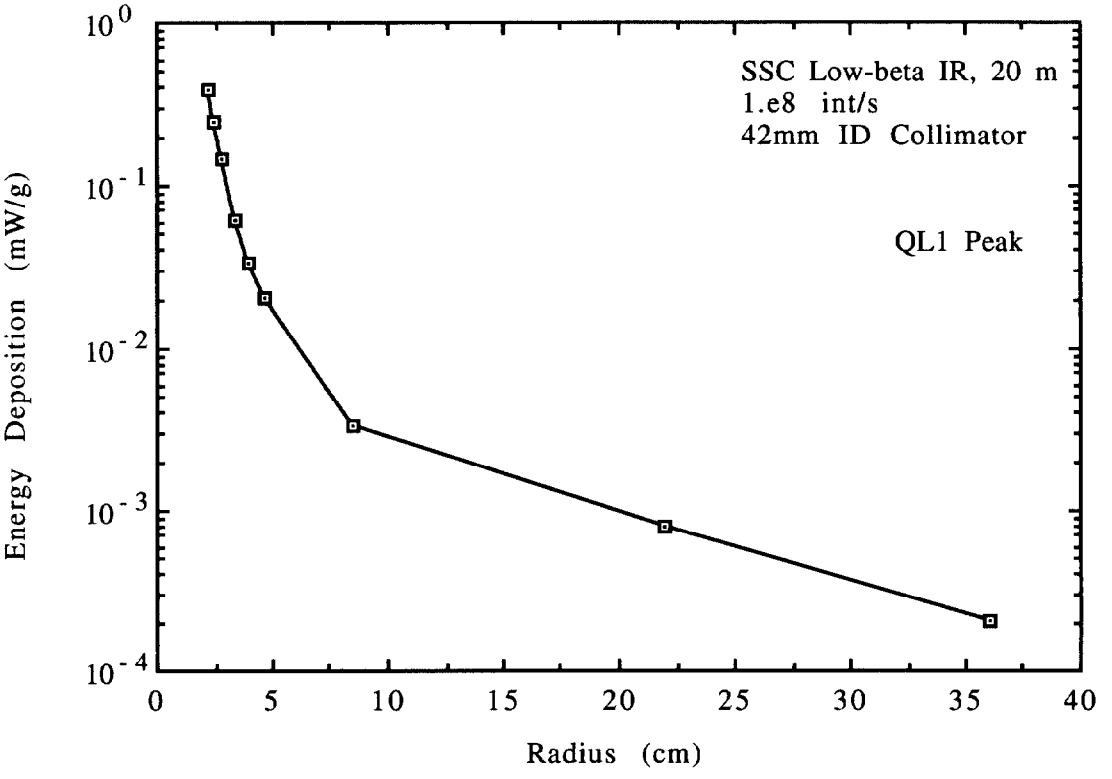
SSC Low-beta IR, 20 m
1.e8 int/s
42mm ID Collimator
QL1 Peak
Energy Deposition (mW/g)
Radius (cm)
10^0
10^-1
10^-2
10^-3
10^-4
0
5
10
15
20
25
30
35
40

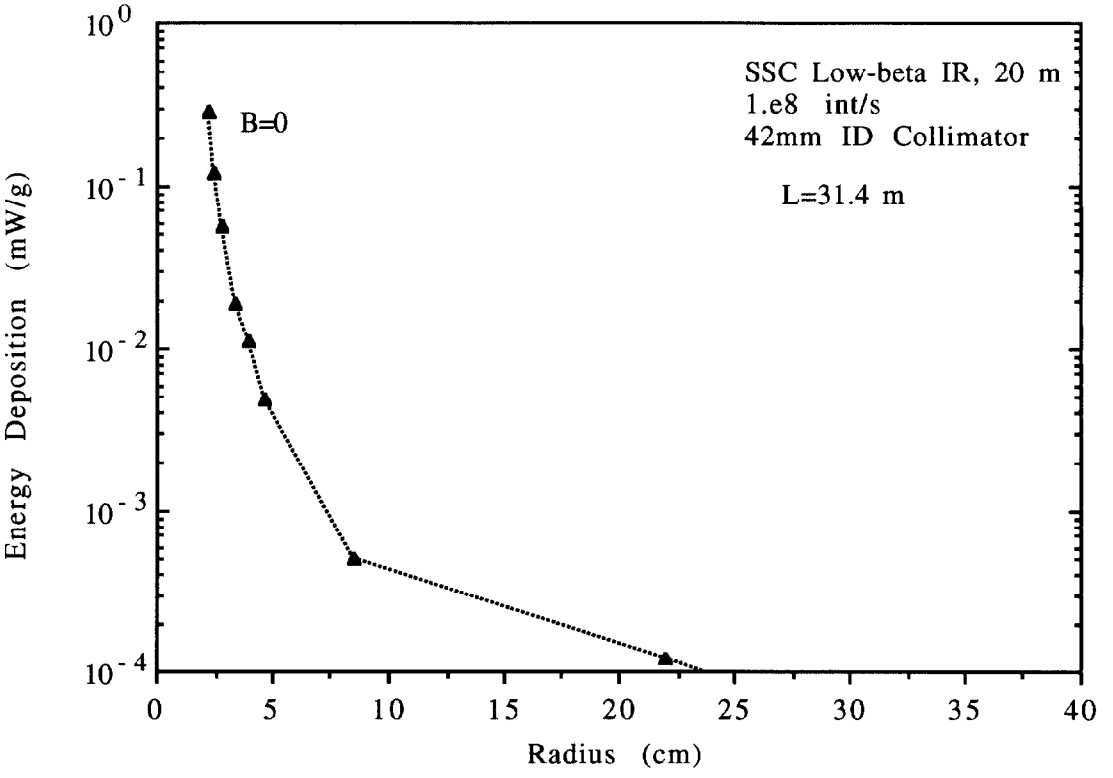
SSC Low-beta IR, 20 m
1.e8 int/s
42mm ID Collimator
L=31.4 m
B=0
Energy Deposition (mW/g)
Radius (cm)
10^0
10^-1
10^-2
10^-3
10^-4
0
5
10
15
20
25
30
35
40

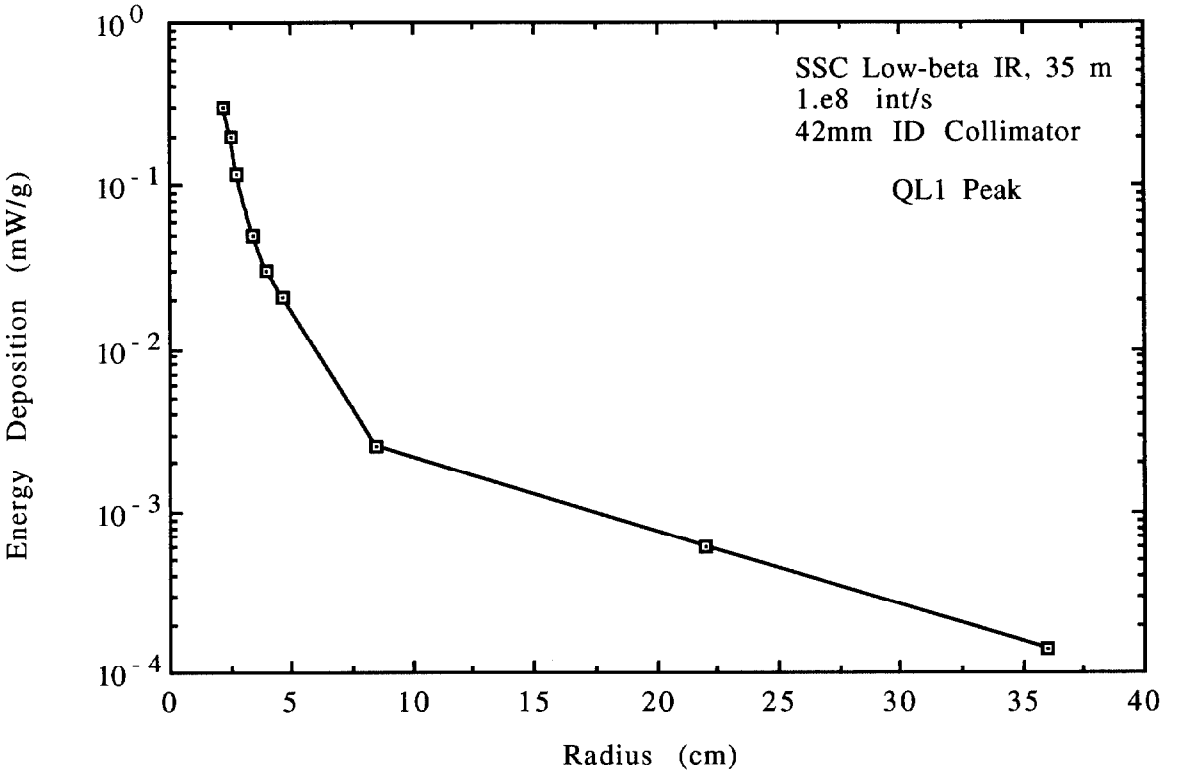
SSC Low-beta IR, 35 m
1.e8 int/s
42mm ID Collimator
QL1 Peak
Energy Deposition (mW/g)
Radius (cm)
10^0
10^-1
10^-2
10^-3
10^-4
0
5
10
15
20
25
30
35
40

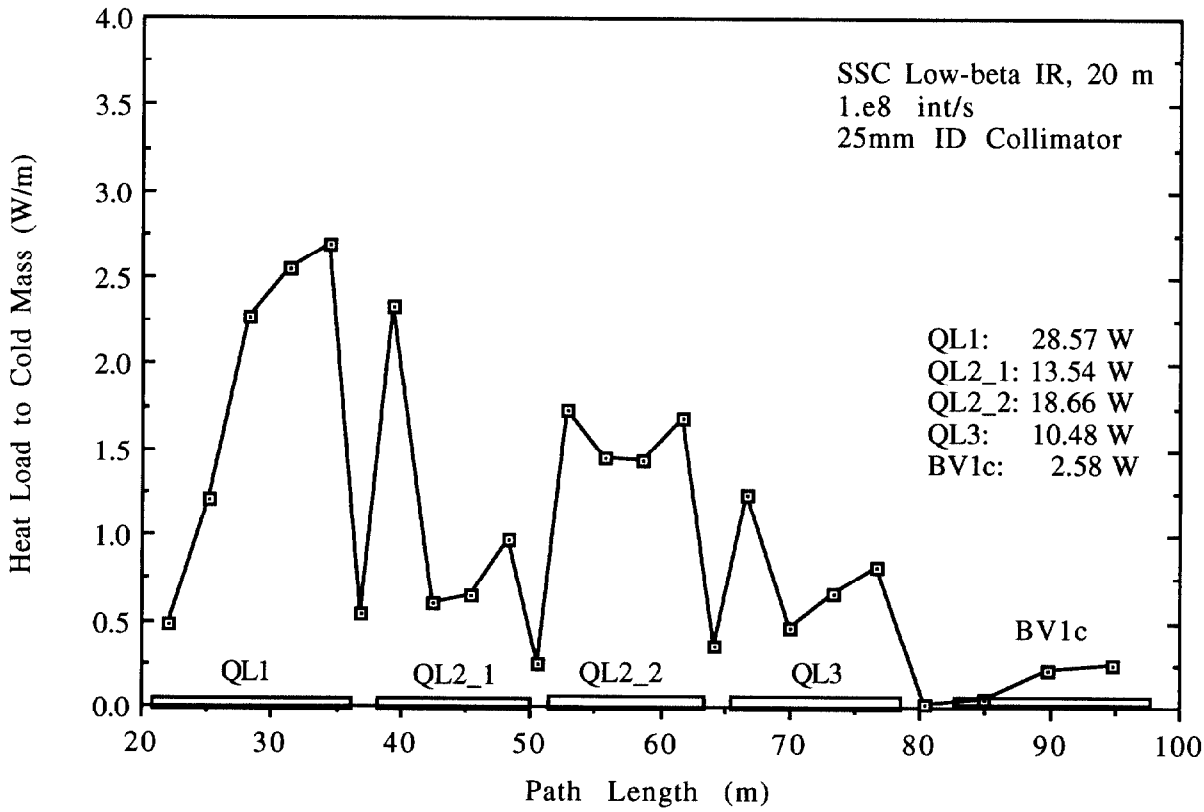
SSC Low-beta IR, 20 m
1.e8 int/s
25mm ID Collimator
QL1: 28.57 W
QL2_1: 13.54 W
QL2_2: 18.66 W
QL3: 10.48 W
BV1c: 2.58 W
QL1
QL2_1
QL2_2
QL3
BV1c
Heat Load to Cold Mass (W/m)
Path Length (m)
4.0
3.5
3.0
2.5
2.0
1.5
1.0
0.5
0.0
20
30
40
50
60
70
80
90
100

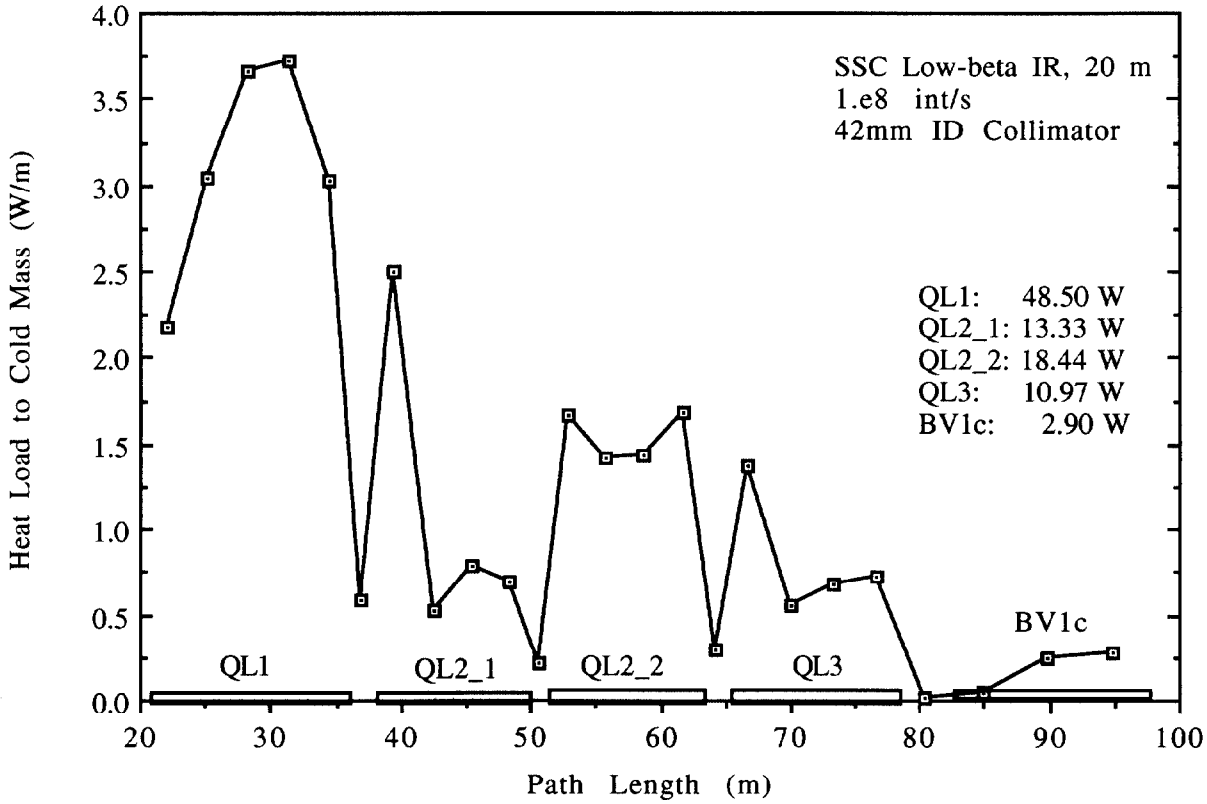
SSC Low-beta IR, 20 m
1.e8 int/s
42mm ID Collimator
QL1: 48.50 W
QL2_1: 13.33 W
QL2_2: 18.44 W
QL3: 10.97 W
BV1c: 2.90 W
QL1
QL2_1
QL2_2
QL3
BV1c
Heat Load to Cold Mass (W/m)
Path Length (m)
4.0
3.5
3.0
2.5
2.0
1.5
1.0
0.5
0.0
20
30
40
50
60
70
80
90
100

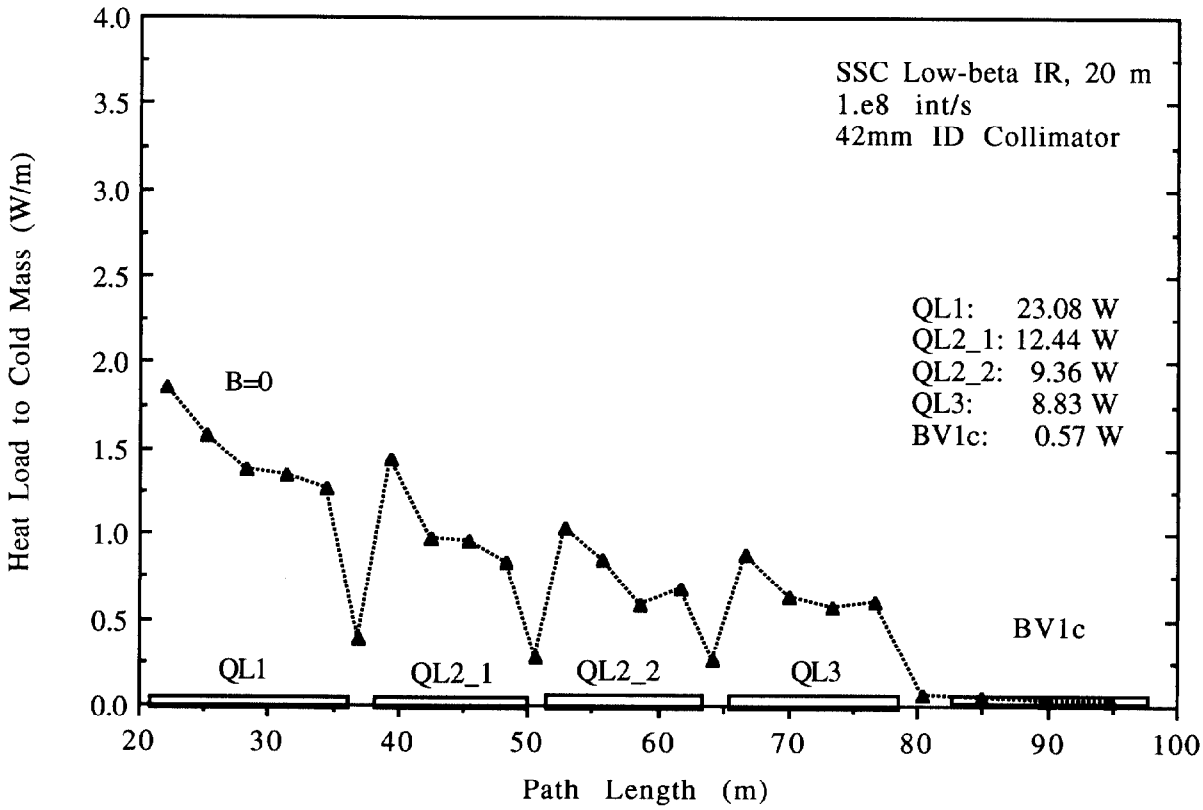
SSC Low-beta IR, 20 m
1.e8 int/s
42mm ID Collimator
QL1: 23.08 W
QL2_1: 12.44 W
QL2_2: 9.36 W
QL3: 8.83 W
BV1c: 0.57 W
B=0
QL1
QL2_1
QL2_2
QL3
BV1c
Heat Load to Cold Mass (W/m)
Path Length (m)
4.0
3.5
3.0
2.5
2.0
1.5
1.0
0.5
0.0
20
30
40
50
60
70
80
90
100

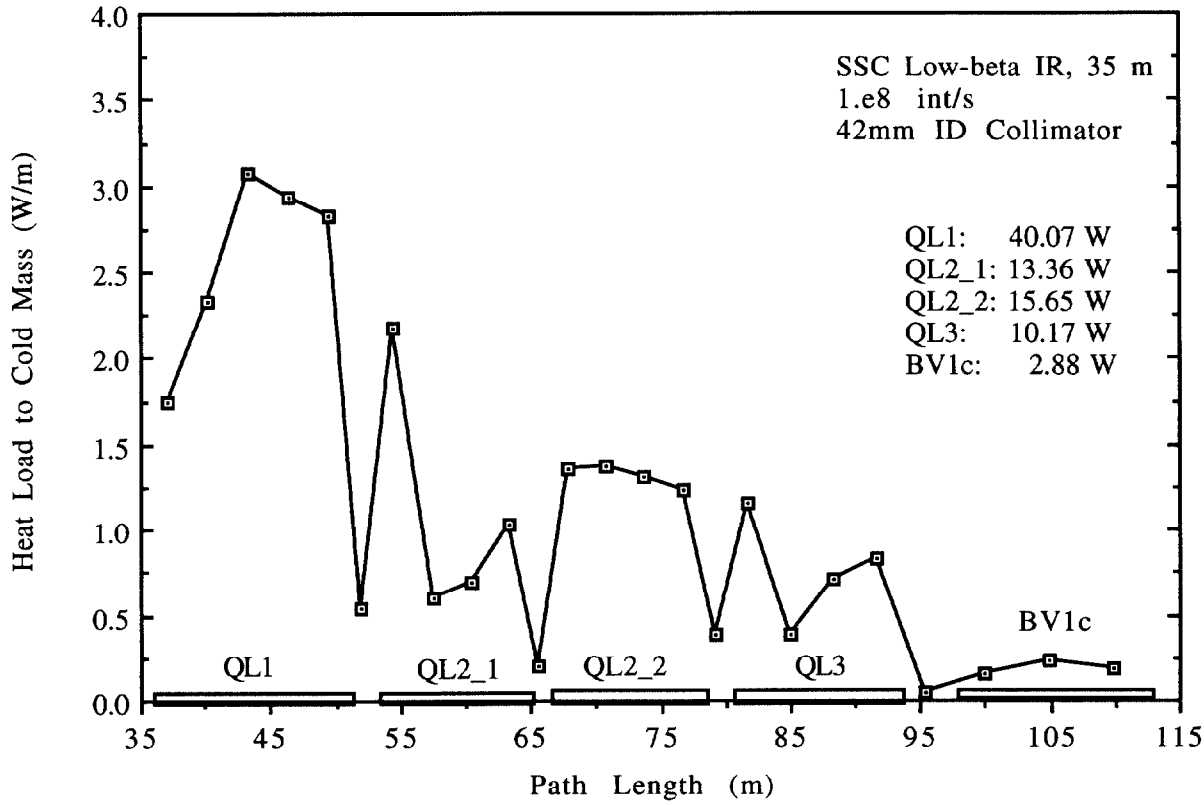
SSC Low-beta IR, 35 m
1.e8 int/s
42mm ID Collimator
QL1: 40.07 W
QL2_1: 13.36 W
QL2_2: 15.65 W
QL3: 10.17 W
BV1c: 2.88 W
Heat Load to Cold Mass (W/m)
Path Length (m)
QL1
QL2_1
QL2_2
QL3
BV1c
4.0
3.5
3.0
2.5
2.0
1.5
1.0
0.5
0.0
35
45
55
65
75
85
95
105
115

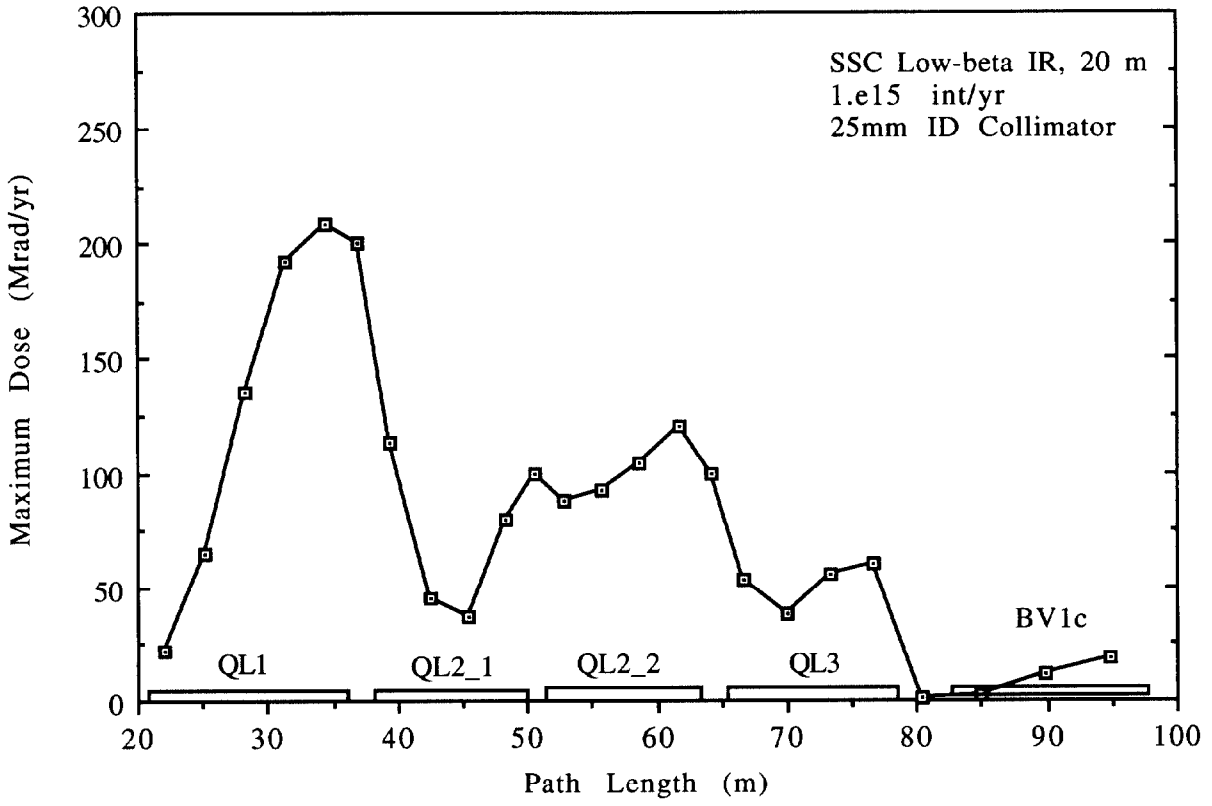
SSC Low-beta IR, 20 m
1.e15 int/yr
25mm ID Collimator
Maximum Dose (Mrad/yr)
Path Length (m)
QL1
QL2_1
QL2_2
QL3
BV1c
300
250
200
150
100
50
0
20
30
40
50
60
70
80
90
100

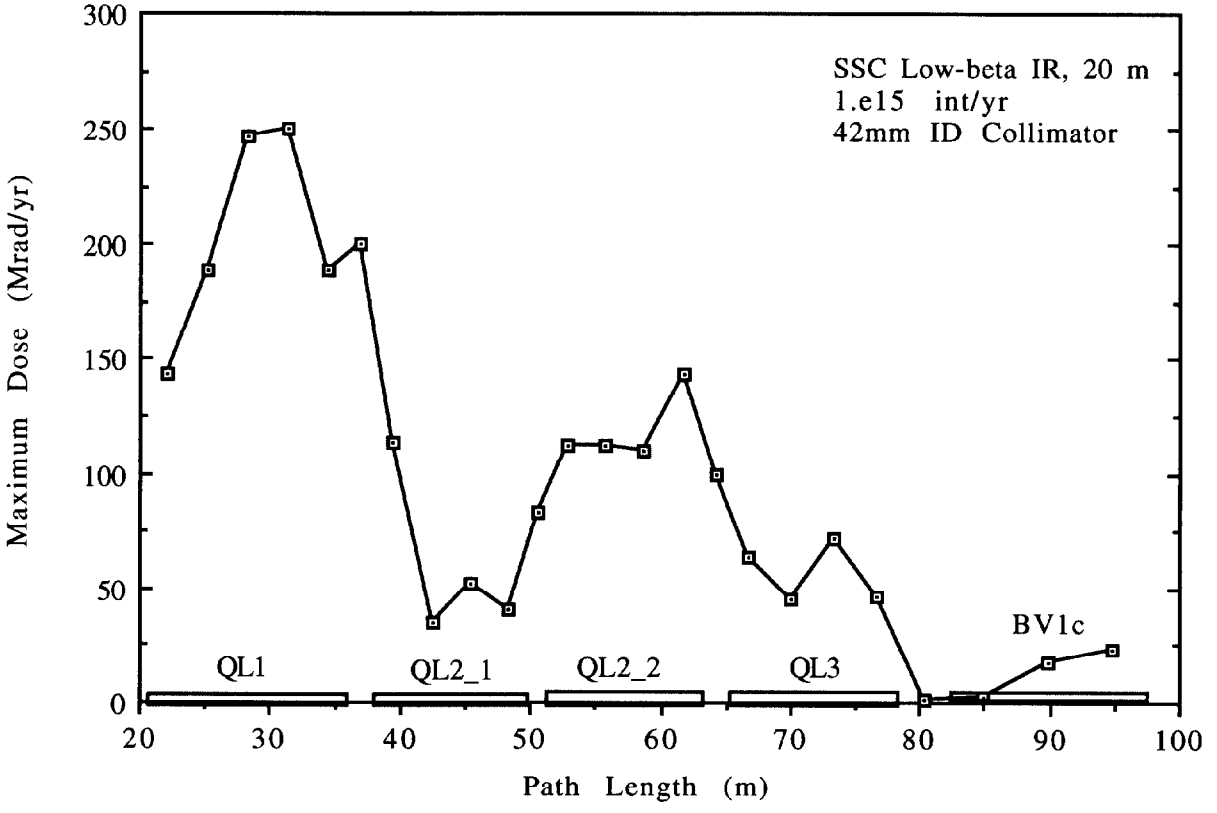
SSC Low-beta IR, 20 m
1.e15 int/yr
42mm ID Collimator
Maximum Dose (Mrad/yr)
Path Length (m)
QL1
QL2_1
QL2_2
QL3
BV1c
300
250
200
150
100
50
0
20
30
40
50
60
70
80
90
100

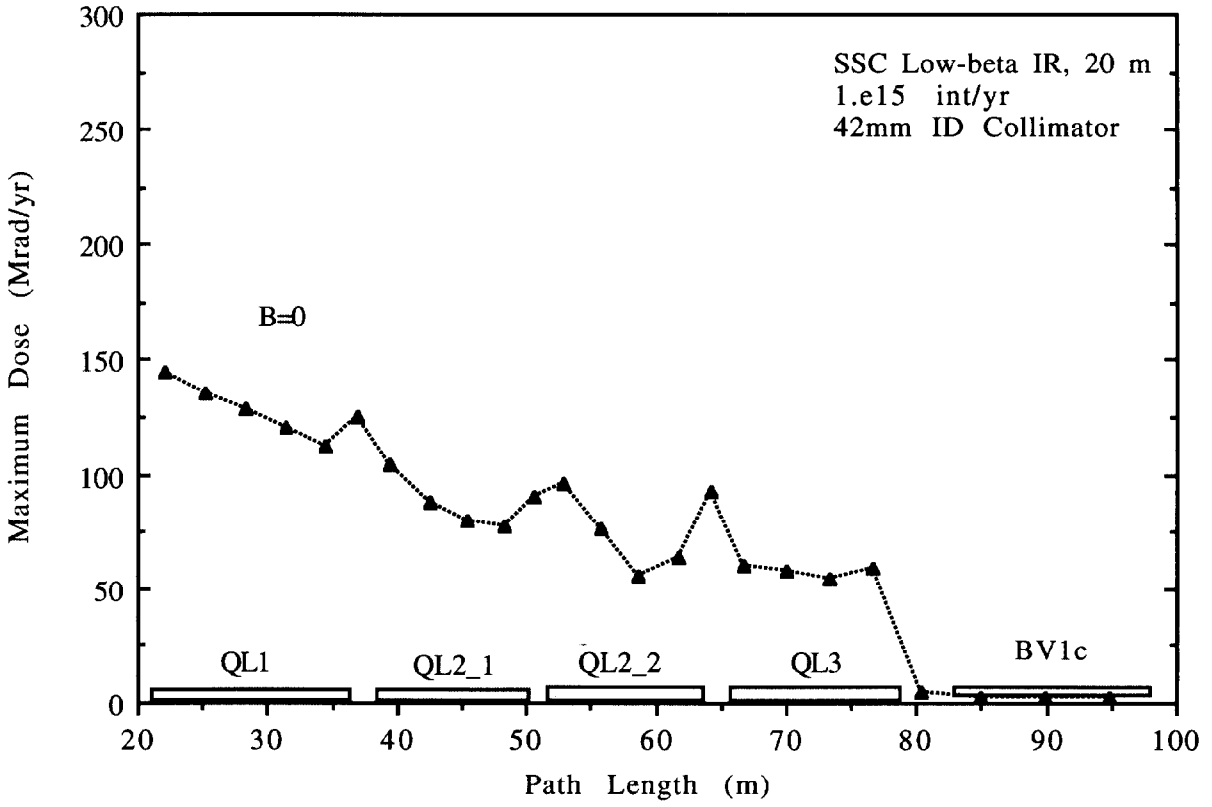
SSC Low-beta IR, 20 m
1.e15 int/yr
42mm ID Collimator
B=0
QL1
QL2_1
QL2_2
QL3
BV1c
Maximum Dose (Mrad/yr)
Path Length (m)
300
250
200
150
100
50
0
20
30
40
50
60
70
80
90
100

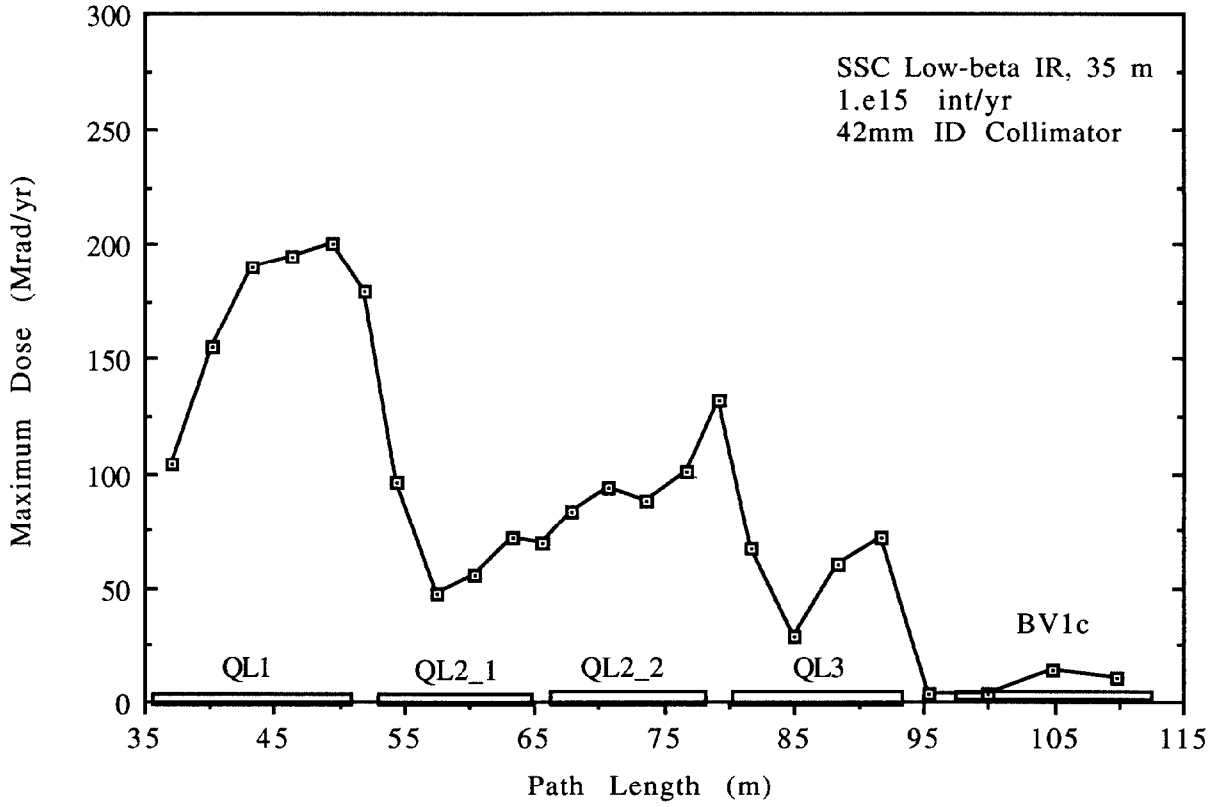
SSC Low-beta IR, 35 m
1.e15 int/yr
42mm ID Collimator
Maximum Dose (Mrad/yr)
300
250
200
150
100
50
0
35
45
55
65
75
85
95
105
115
Path Length (m)
QL1
QL2_1
QL2_2
QL3
BV1c

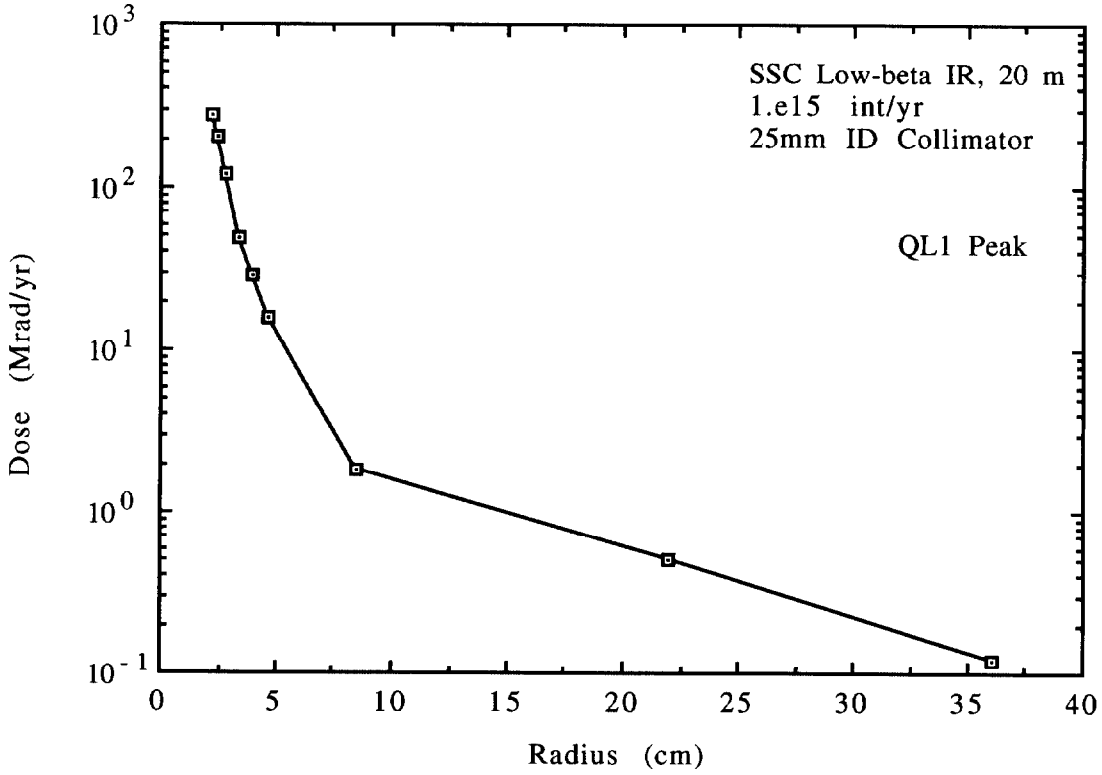
SSC Low-beta IR, 20 m
1.e15 int/yr
25mm ID Collimator
QL1 Peak
Dose (Mrad/yr)
Radius (cm)
10^3
10^2
10^1
10^0
10^{-1}
0
5
10
15
20
25
30
35
40

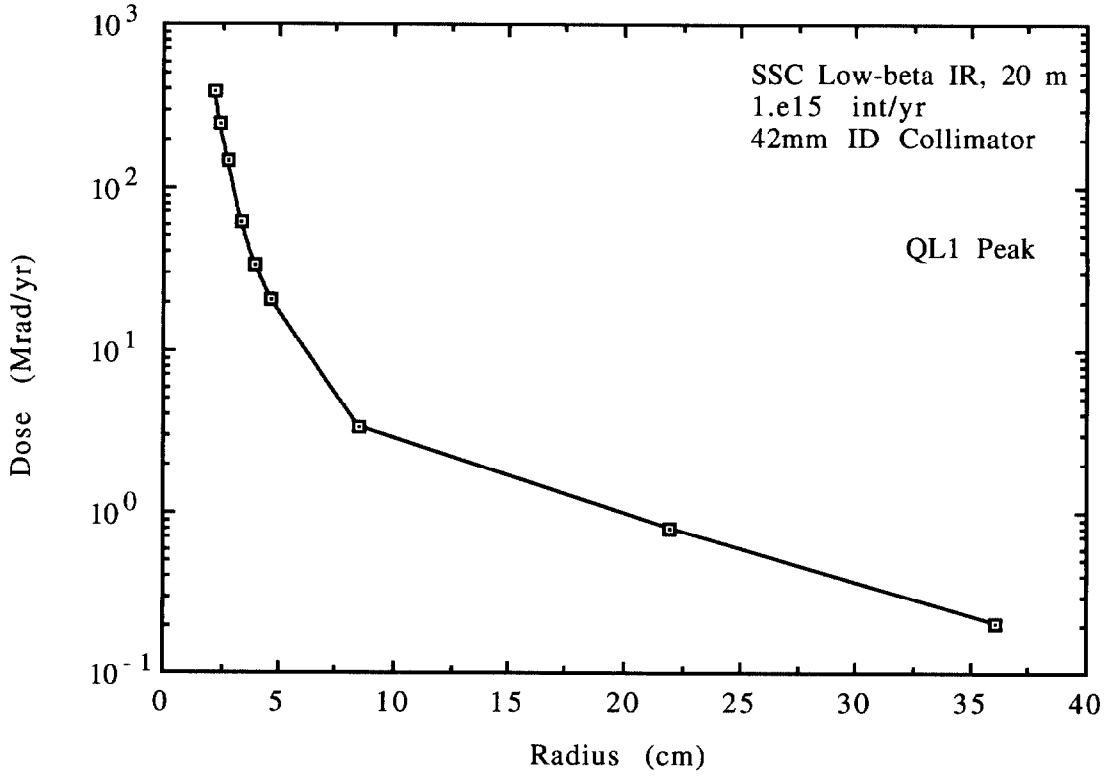
SSC Low-beta IR, 20 m
1.e15 int/yr
42mm ID Collimator
QL1 Peak
Dose (Mrad/yr)
Radius (cm)
10^3
10^2
10^1
10^0
10^{-1}
0
5
10
15
20
25
30
35
40

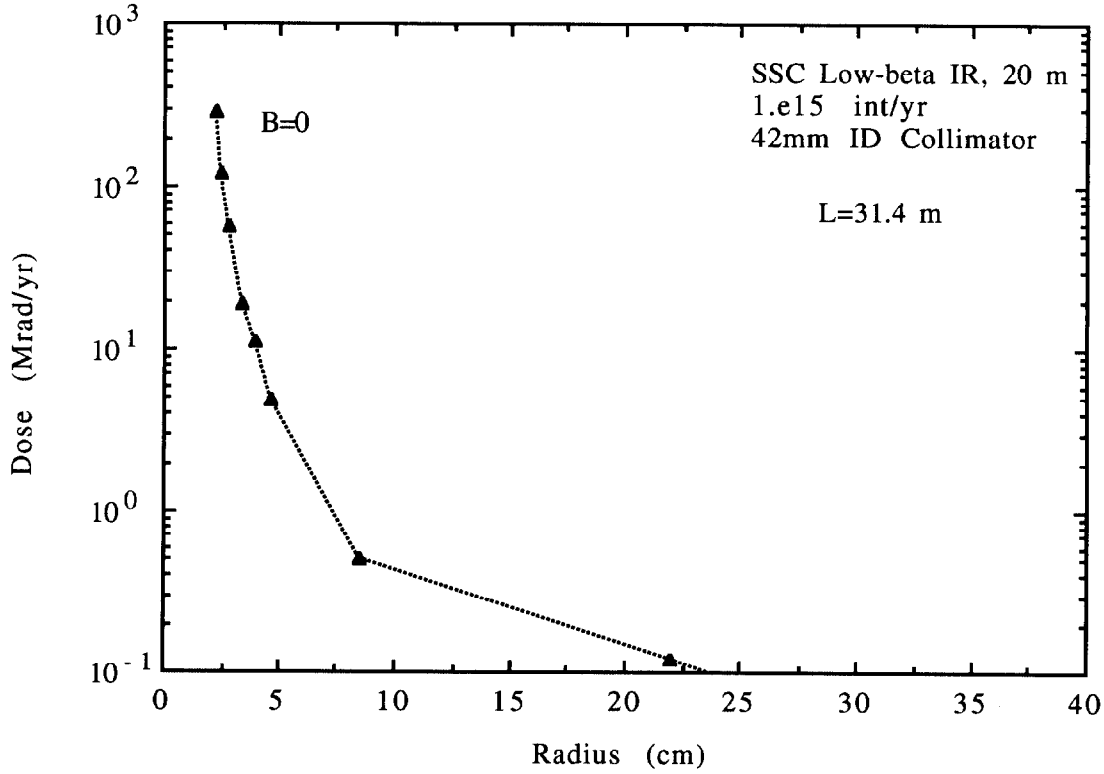
SSC Low-beta IR, 20 m
1.e15 int/yr
42mm ID Collimator
L=31.4 m
B=0
Dose (Mrad/yr)
Radius (cm)
10^3
10^2
10^1
10^0
10^{-1}
0
5
10
15
20
25
30
35
40

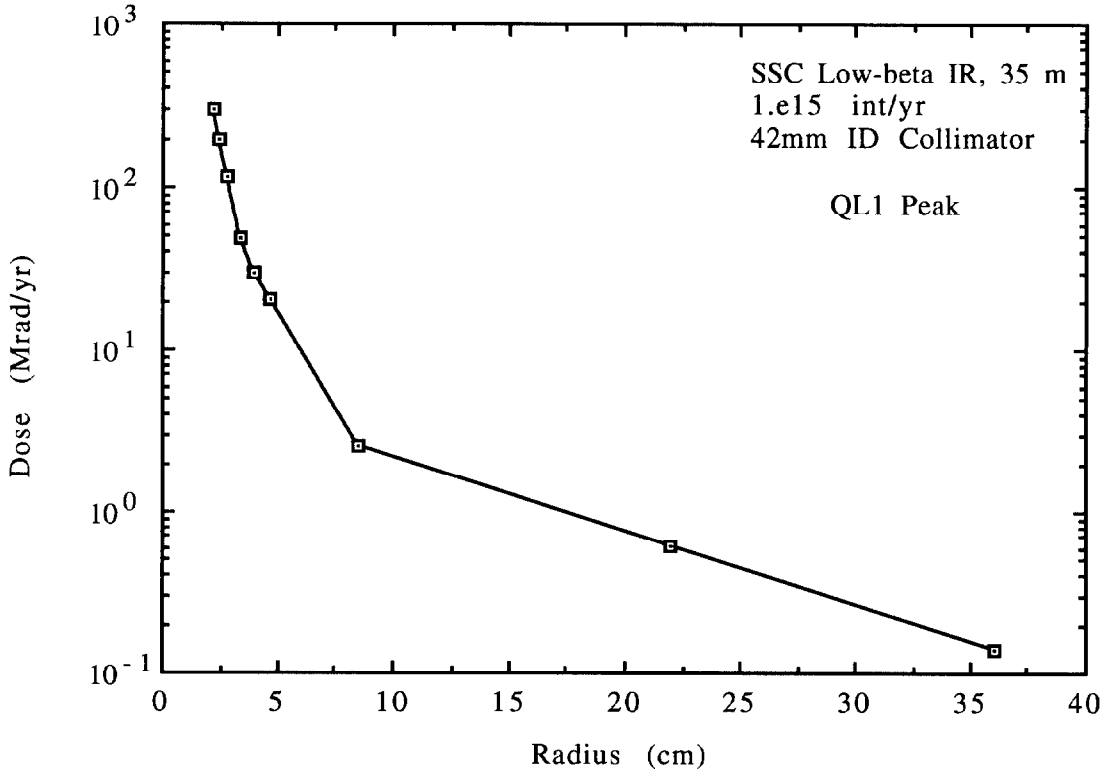
SSC Low-beta IR, 35 m
1.e15 int/yr
42mm ID Collimator
QL1 Peak
Dose (Mrad/yr)
Radius (cm)
10^3
10^2
10^1
10^0
10^{-1}
0
5
10
15
20
25
30
35
40

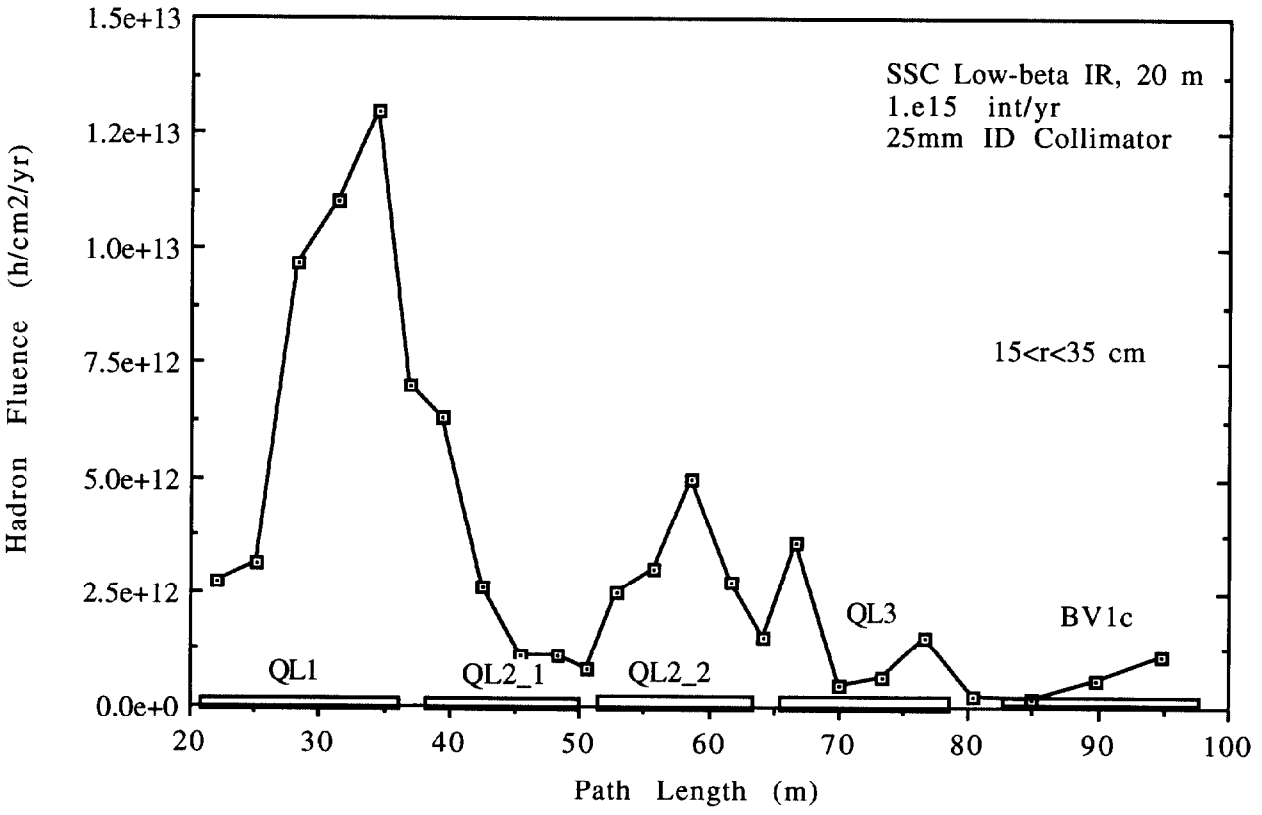
SSC Low-beta IR, 20 m
1.e15 int/yr
25mm ID Collimator
15<r<35 cm
Hadron Fluence (h/cm2/yr)
1.5e+13
1.2e+13
1.0e+13
7.5e+12
5.0e+12
2.5e+12
0.0e+0
QL1
QL2_1
QL2_2
QL3
BV1c
20
30
40
50
60
70
80
90
100
Path Length (m)

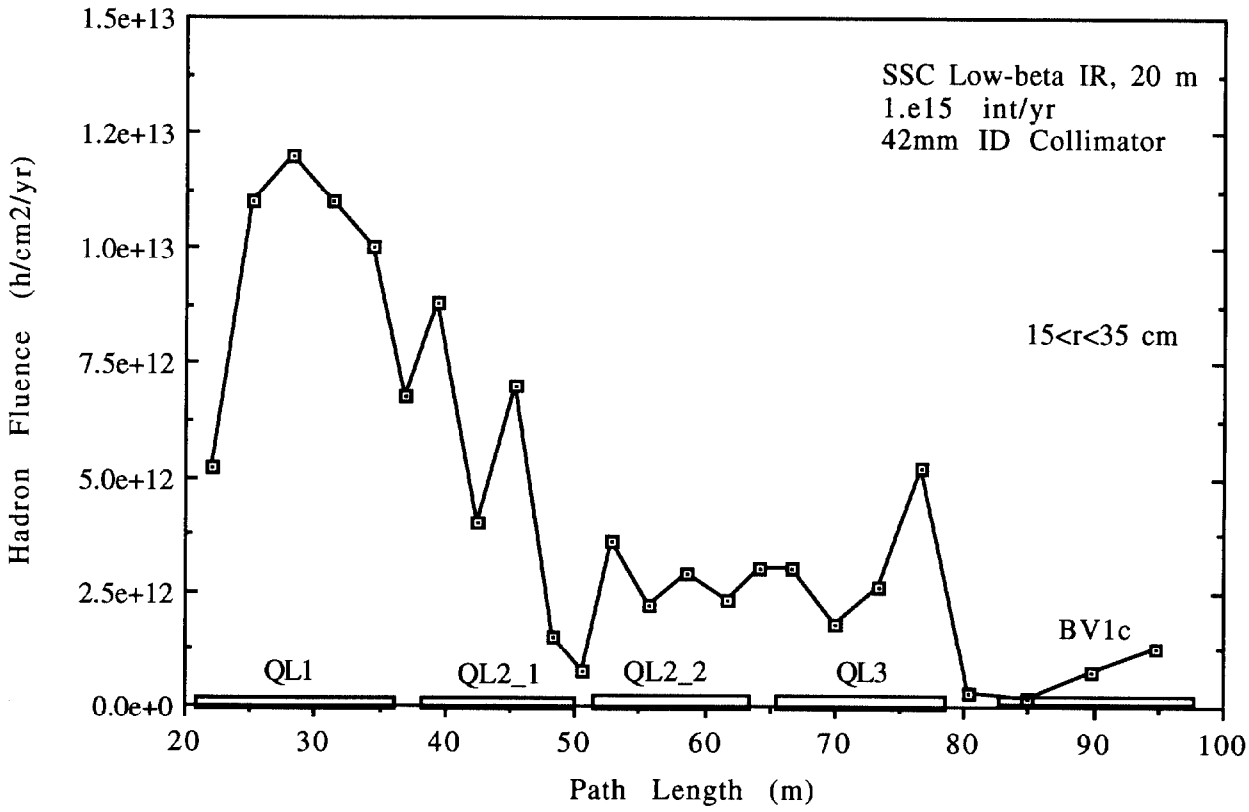
SSC Low-beta IR, 20 m
1.e15 int/yr
42mm ID Collimator
15<r<35 cm
Hadron Fluence (h/cm2/yr)
1.5e+13
1.2e+13
1.0e+13
7.5e+12
5.0e+12
2.5e+12
0.0e+0
QL1
QL2_1
QL2_2
QL3
BV1c
20
30
40
50
60
70
80
90
100
Path Length (m)

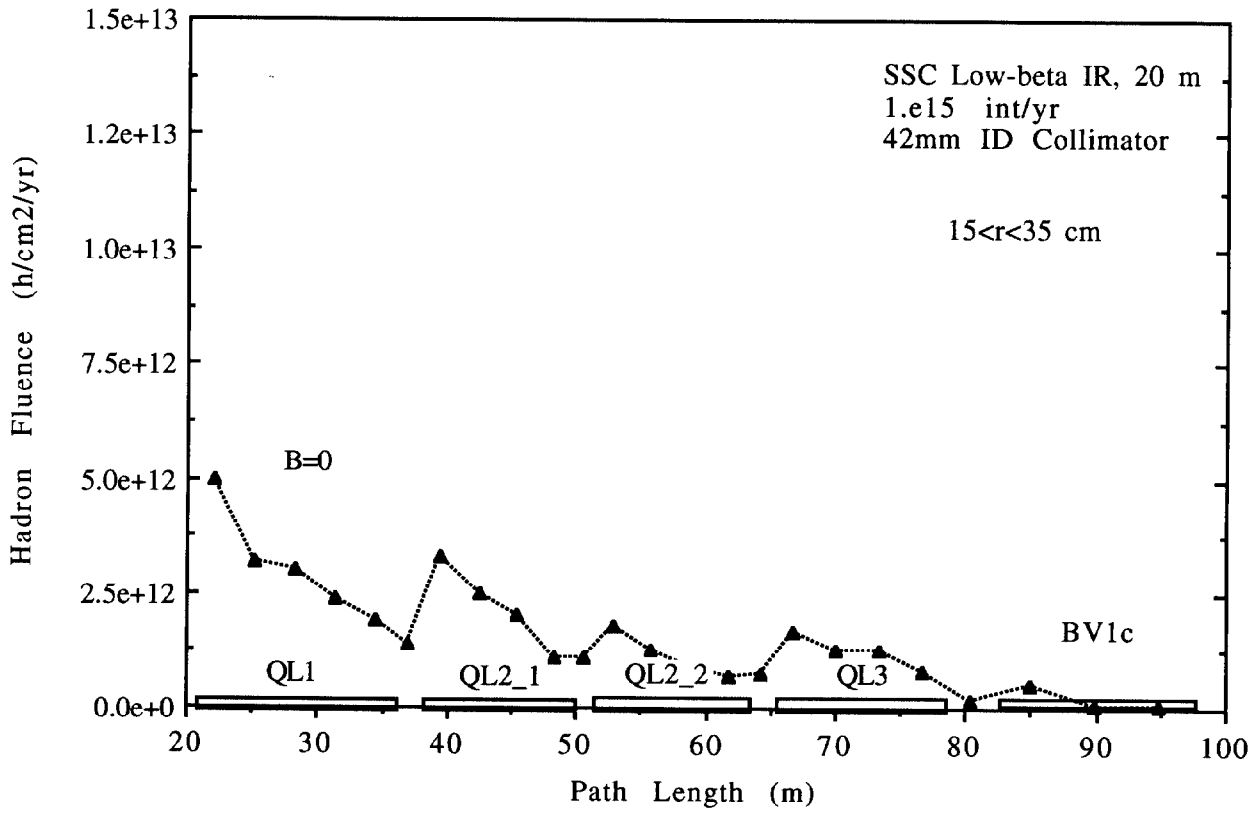
SSC Low-beta IR, 20 m
1.e15 int/yr
42mm ID Collimator
15<r<35 cm
B=0
BV1c
QL1
QL2_1
QL2_2
QL3
Hadron Fluence (h/cm2/yr)
Path Length (m)
1.5e+13
1.2e+13
1.0e+13
7.5e+12
5.0e+12
2.5e+12
0.0e+0
20
30
40
50
60
70
80
90
100

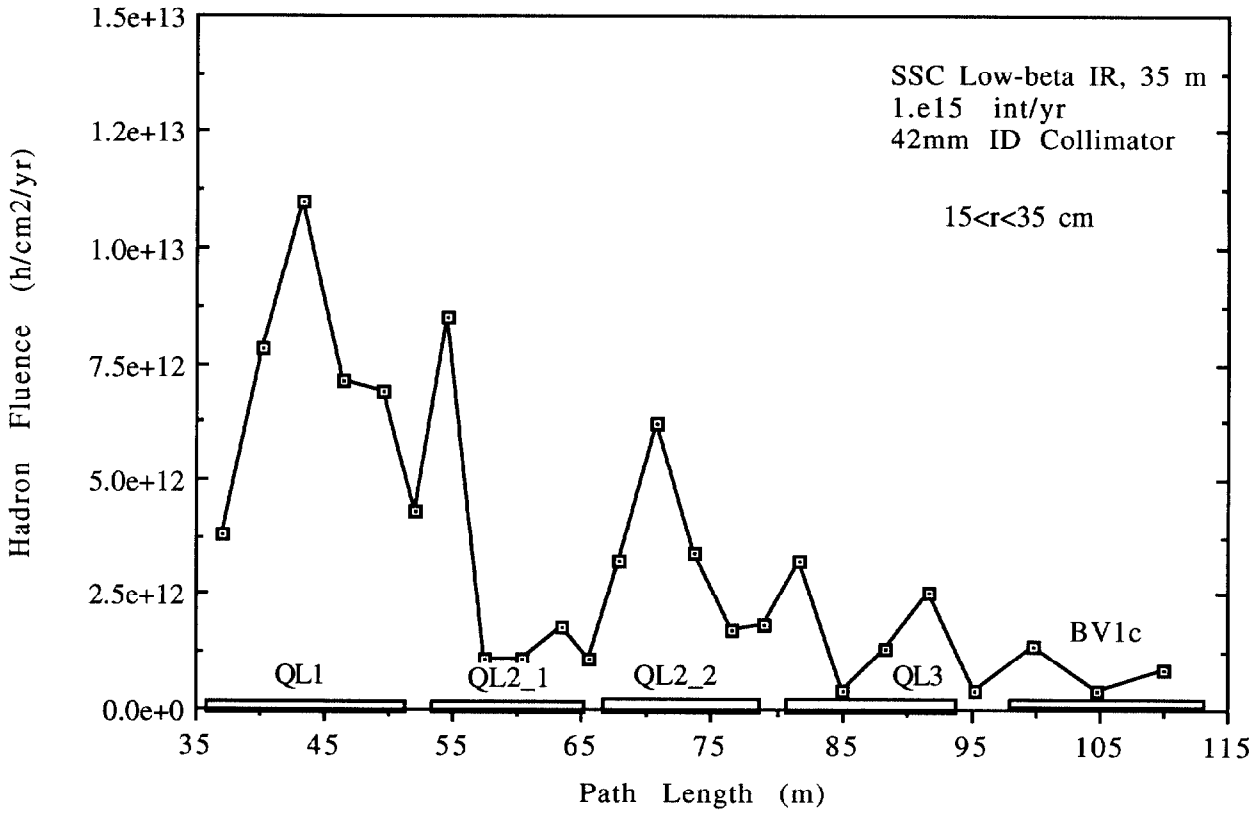
SSC Low-beta IR, 35 m
1.e15 int/yr
42mm ID Collimator
15<r<35 cm
Hadron Fluence (h/cm2/yr)
1.5e+13
1.2e+13
1.0e+13
7.5e+12
5.0e+12
2.5e+12
0.0e+0
QL1
QL2_1
QL2_2
QL3
BV1c
35
45
55
65
75
85
95
105
115
Path Length (m)

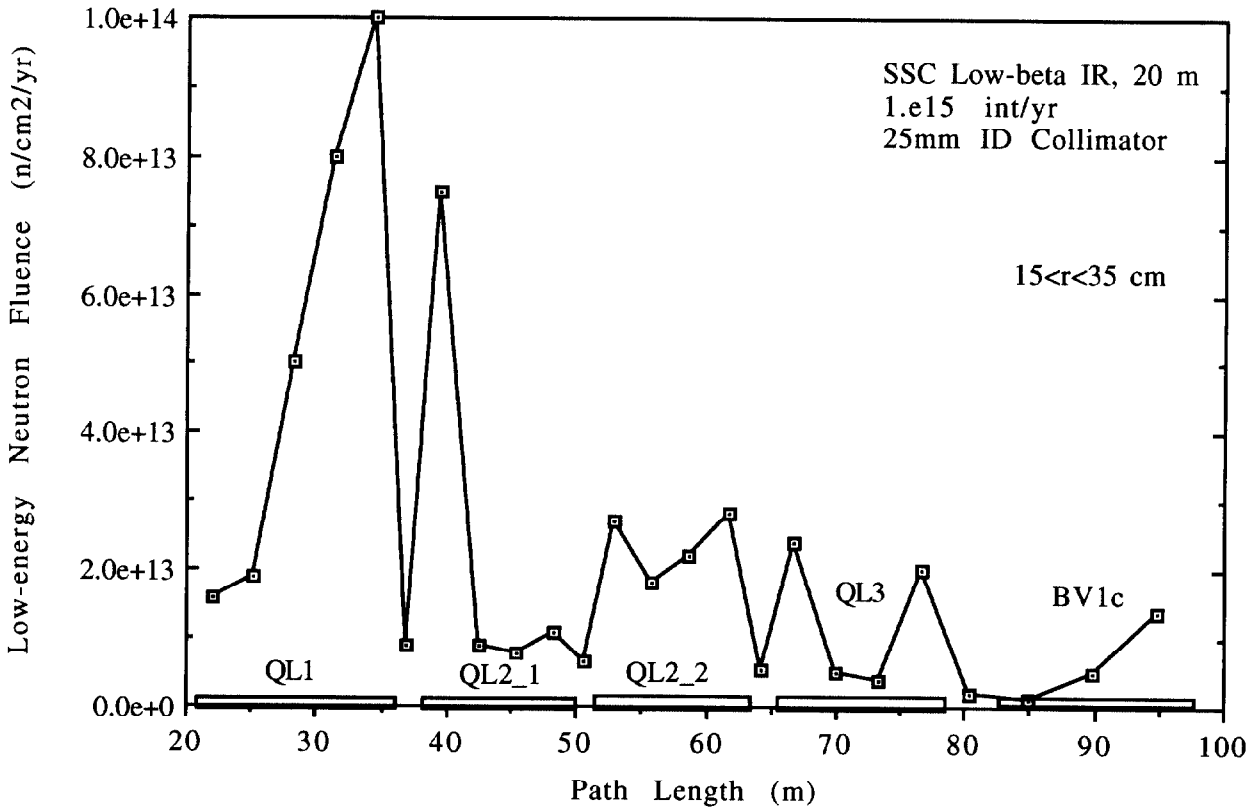
SSC Low-beta IR, 20 m
1.e15 int/yr
25mm ID Collimator
15<r<35 cm
Low-energy Neutron Fluence (n/cm2/yr)
1.0e+14
8.0e+13
6.0e+13
4.0e+13
2.0e+13
0.0e+0
20
30
40
50
60
70
80
90
100
Path Length (m)
QL1
QL2_1
QL2_2
QL3
BV1c

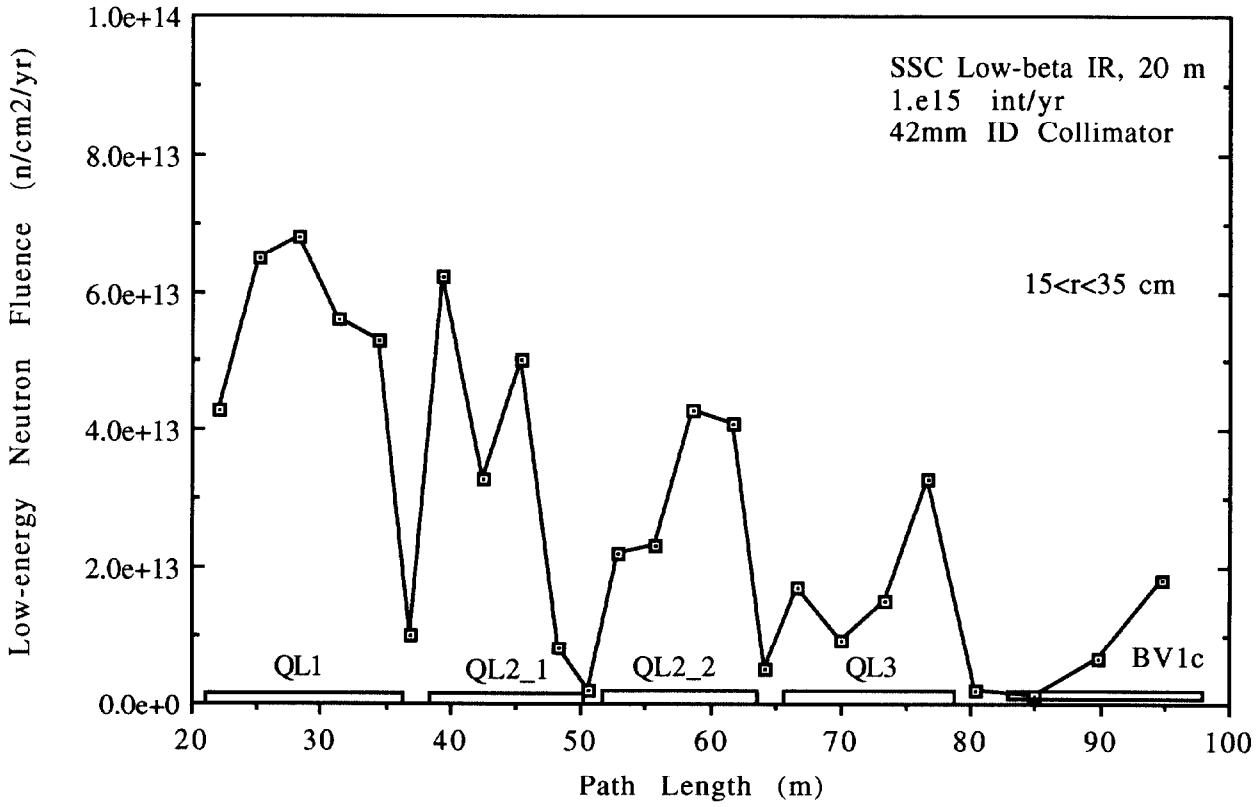
SSC Low-beta IR, 20 m
1.e15 int/yr
42mm ID Collimator
15<r<35 cm
Low-energy Neutron Fluence (n/cm2/yr)
1.0e+14
8.0e+13
6.0e+13
4.0e+13
2.0e+13
0.0e+0
QL1
QL2_1
QL2_2
QL3
BV1c
20
30
40
50
60
70
80
90
100
Path Length (m)

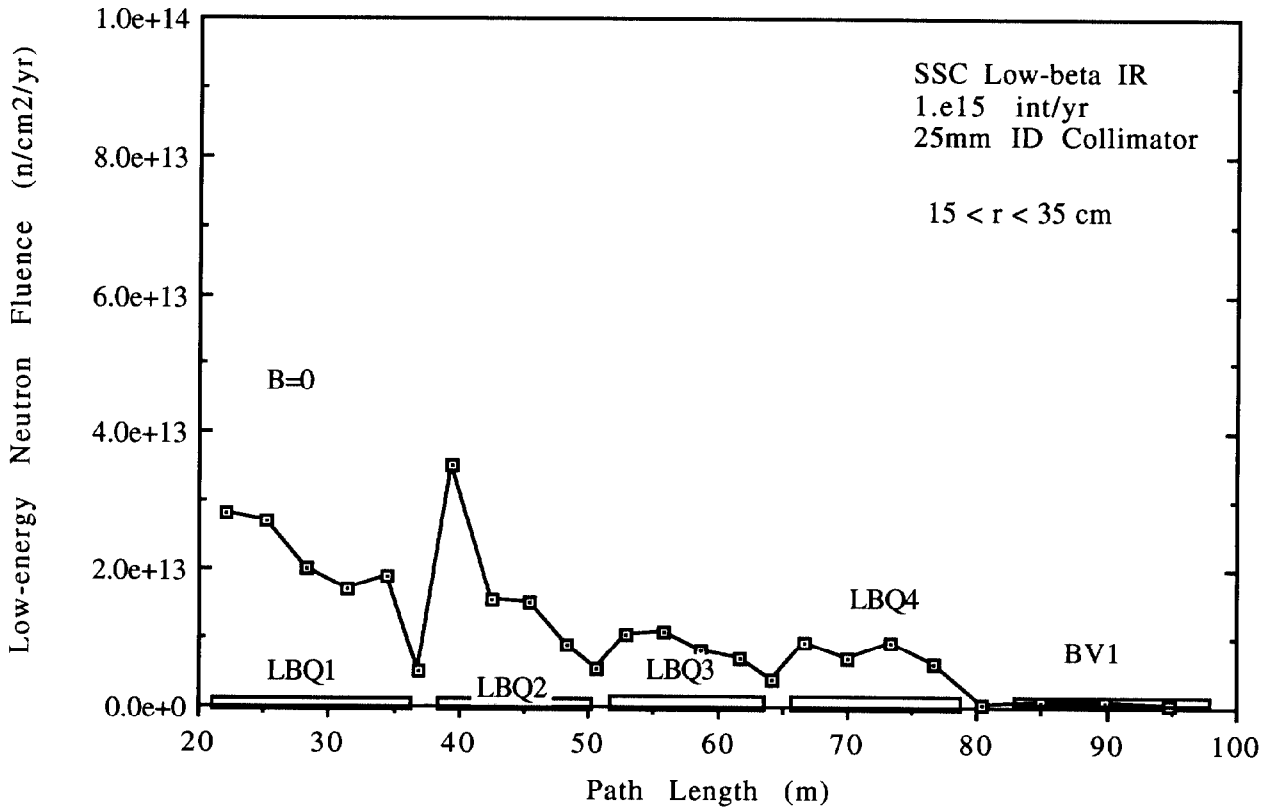
SSC Low-beta IR
1.e15 int/yr
25mm ID Collimator
15 < r < 35 cm
B=0
LBQ1
LBQ2
LBQ3
LBQ4
BV1
Low-energy Neutron Fluence (n/cm2/yr)
1.0e+14
8.0e+13
6.0e+13
4.0e+13
2.0e+13
0.0e+0
20
30
40
50
60
70
80
90
100
Path Length (m)

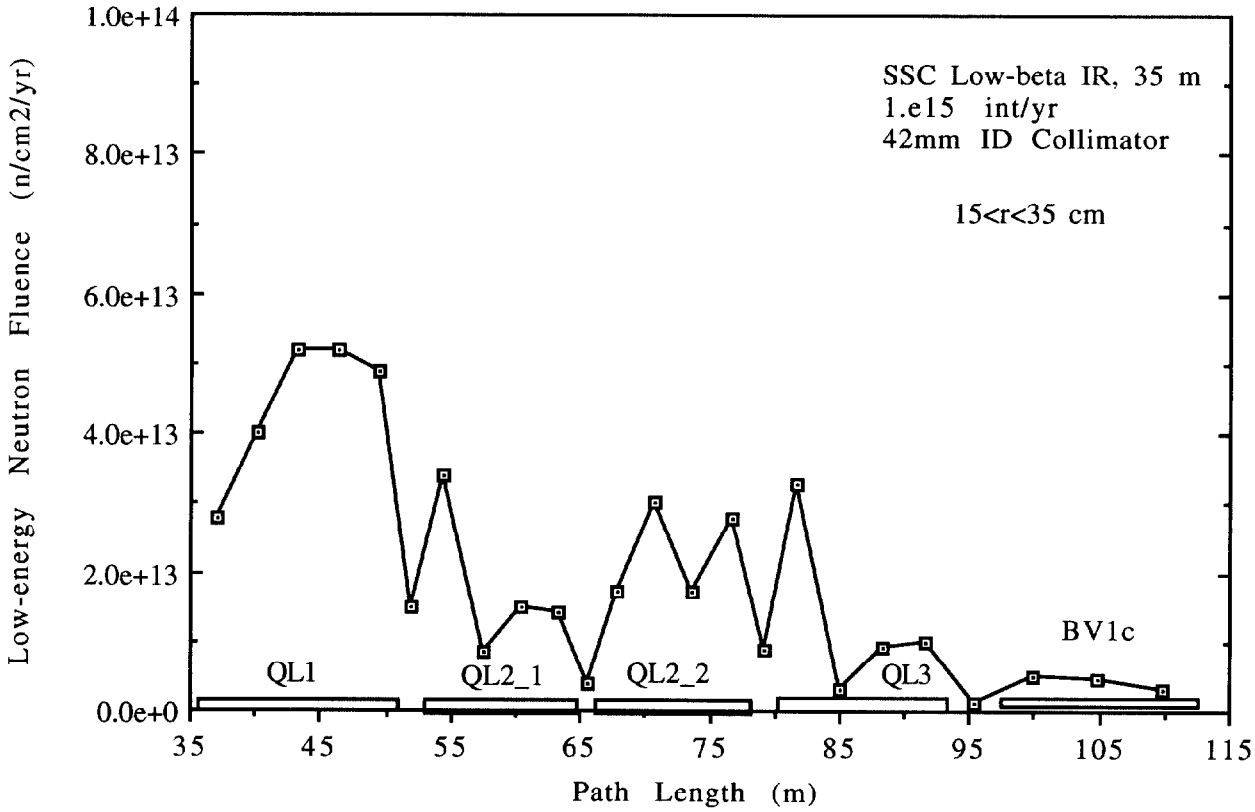
SSC Low-beta IR, 35 m
1.e15 int/yr
42mm ID Collimator
15<r<35 cm
Low-energy Neutron Fluence (n/cm2/yr)
1.0e+14
8.0e+13
6.0e+13
4.0e+13
2.0e+13
0.0e+0
QL1
QL2_1
QL2_2
QL3
BV1c
35
45
55
65
75
85
95
105
115
Path Length (m)

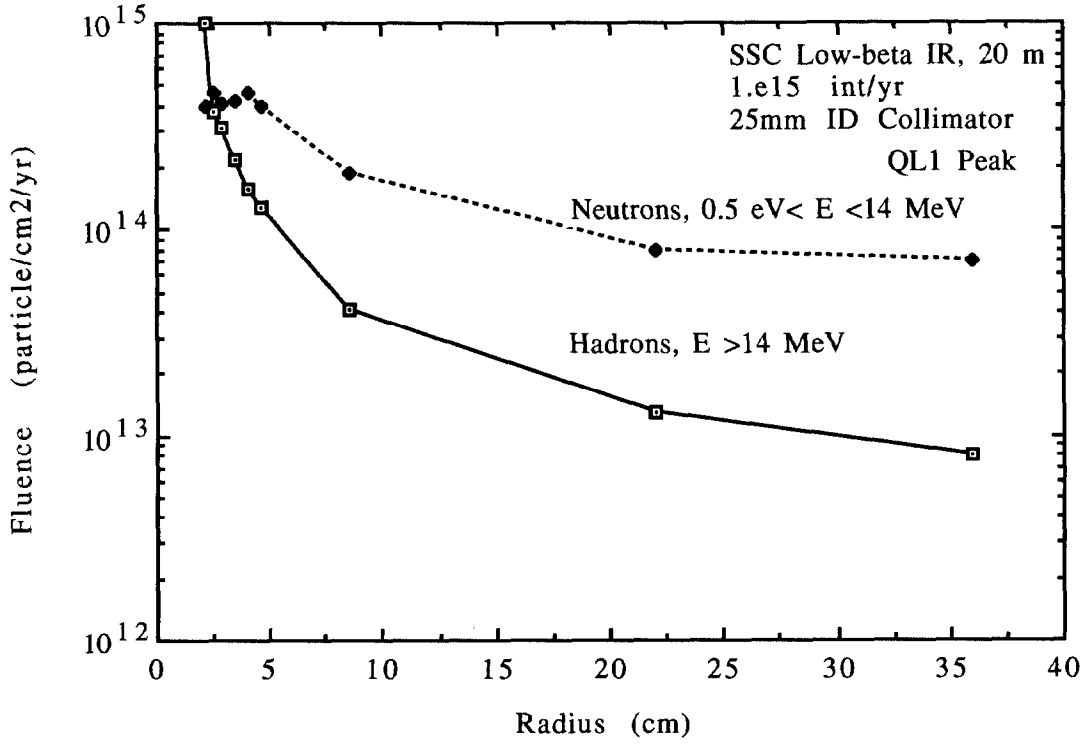
SSC Low-beta IR, 20 m
1.e15 int/yr
25mm ID Collimator
QL1 Peak
Neutrons, 0.5 eV< E <14 MeV
Hadrons, E >14 MeV
Fluence (particle/cm2/yr)
Radius (cm)
10^15
10^14
10^13
10^12
0
5
10
15
20
25
30
35
40

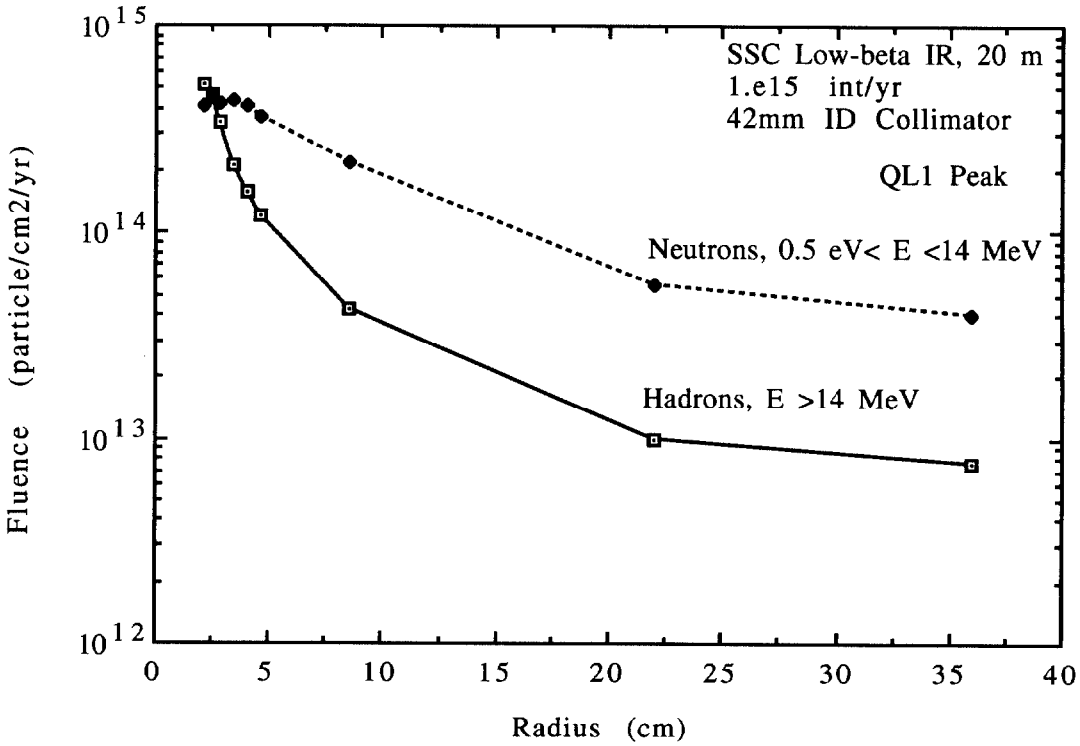
SSC Low-beta IR, 20 m
1.e15 int/yr
42mm ID Collimator
QL1 Peak
Neutrons, 0.5 eV< E <14 MeV
Hadrons, E >14 MeV
Fluence (particle/cm2/yr)
Radius (cm)
10^15
10^14
10^13
10^12
0
5
10
15
20
25
30
35
40

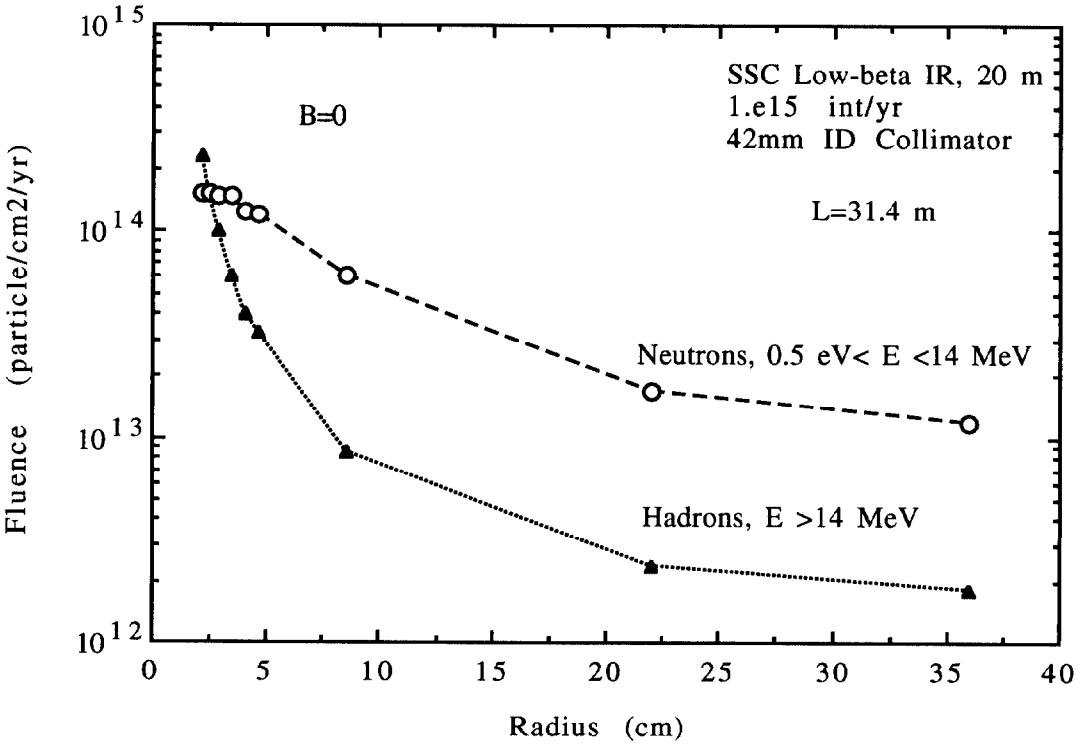
SSC Low-beta IR, 20 m
1.e15 int/yr
42mm ID Collimator
L=31.4 m
B=0
Neutrons, 0.5 eV< E <14 MeV
Hadrons, E >14 MeV
Fluence (particle/cm2/yr)
Radius (cm)
10^15
10^14
10^13
10^12
0
5
10
15
20
25
30
35
40

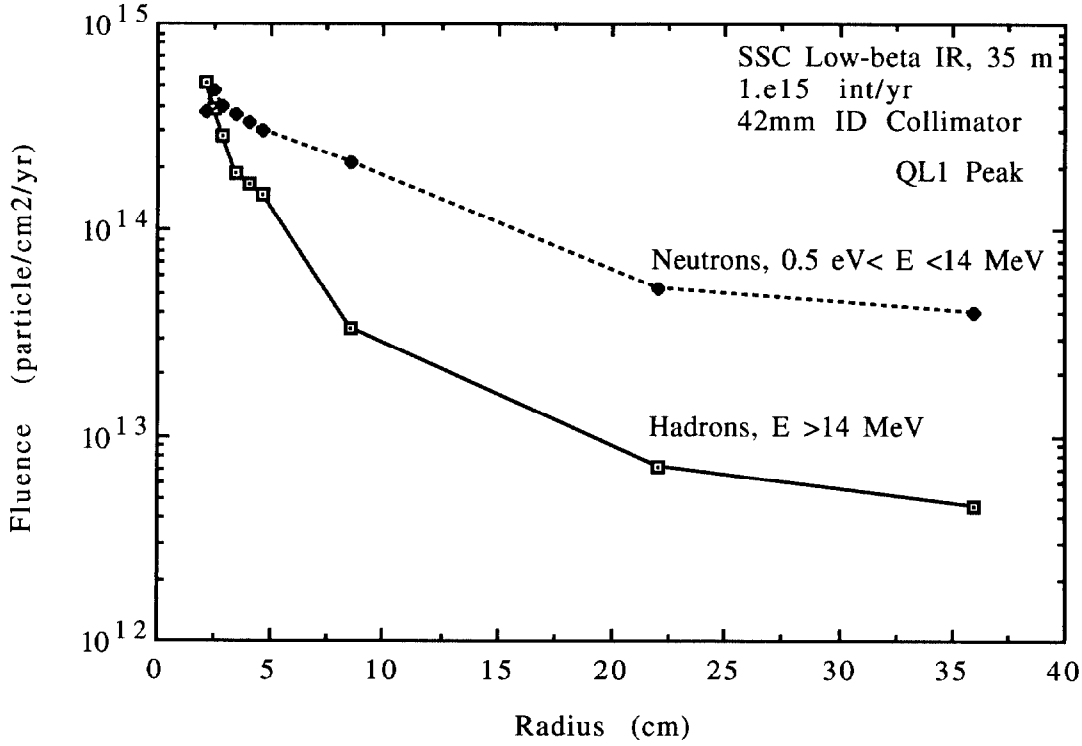
SSC Low-beta IR, 35 m
1.e15 int/yr
42mm ID Collimator
QL1 Peak
Neutrons, 0.5 eV< E <14 MeV
Hadrons, E >14 MeV
Fluence (particle/cm2/yr)
Radius (cm)
10^15
10^14
10^13
10^12
0
5
10
15
20
25
30
35
40

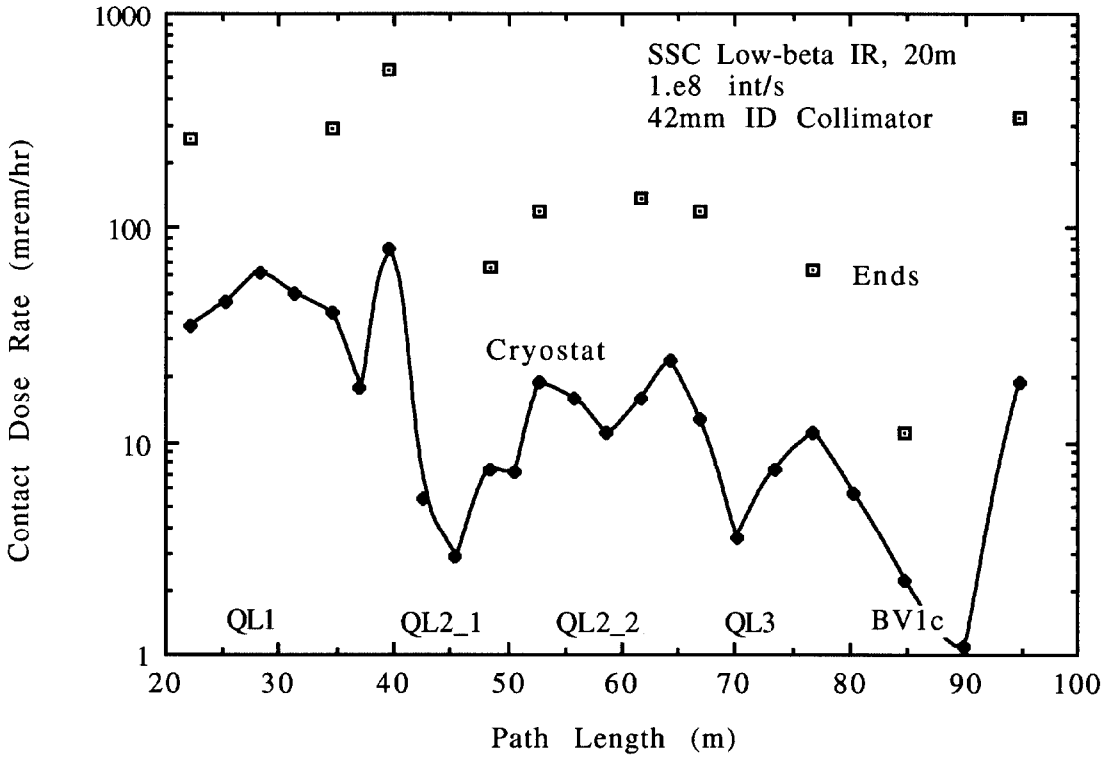
SSC Low-beta IR, 20m
1.e8 int/s
42mm ID Collimator
Ends
Cryostat
QL1
QL2_1
QL2_2
QL3
BV1c
Contact Dose Rate (mrem/hr)
Path Length (m)
1000
100
10
1
20
30
40
50
60
70
80
90
100

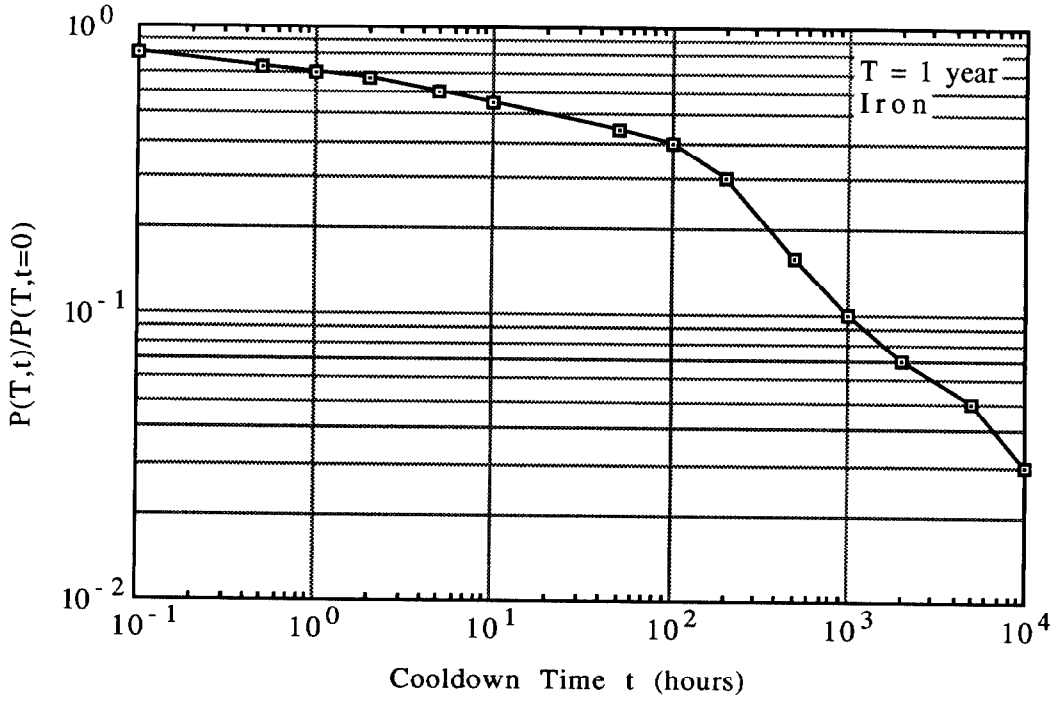
10^0
10^{-1}
10^{-2}
P(T,t)/P(T,t=0)
T = 1 year
Iron
10^{-1}
10^0
10^1
10^2
10^3
10^4
Cooldown Time t (hours)

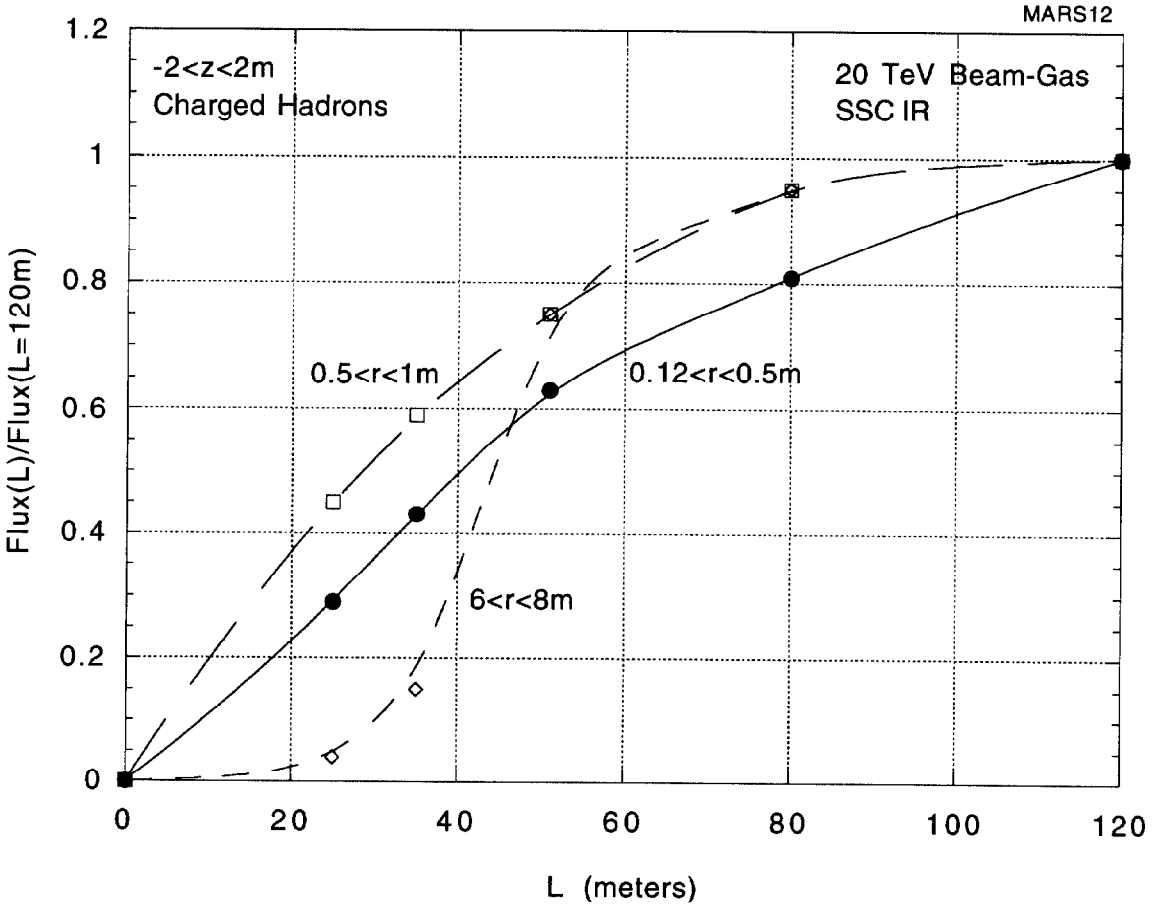
MARS12
-2<z<2m
Charged Hadrons
20 TeV Beam-Gas
SSC IR
0.5<r<1m
0.12<r<0.5m
6<r<8m
Flux(L)/Flux(L=120m)
L (meters)
0
0.2
0.4
0.6
0.8
1
1.2
0
20
40
60
80
100
120

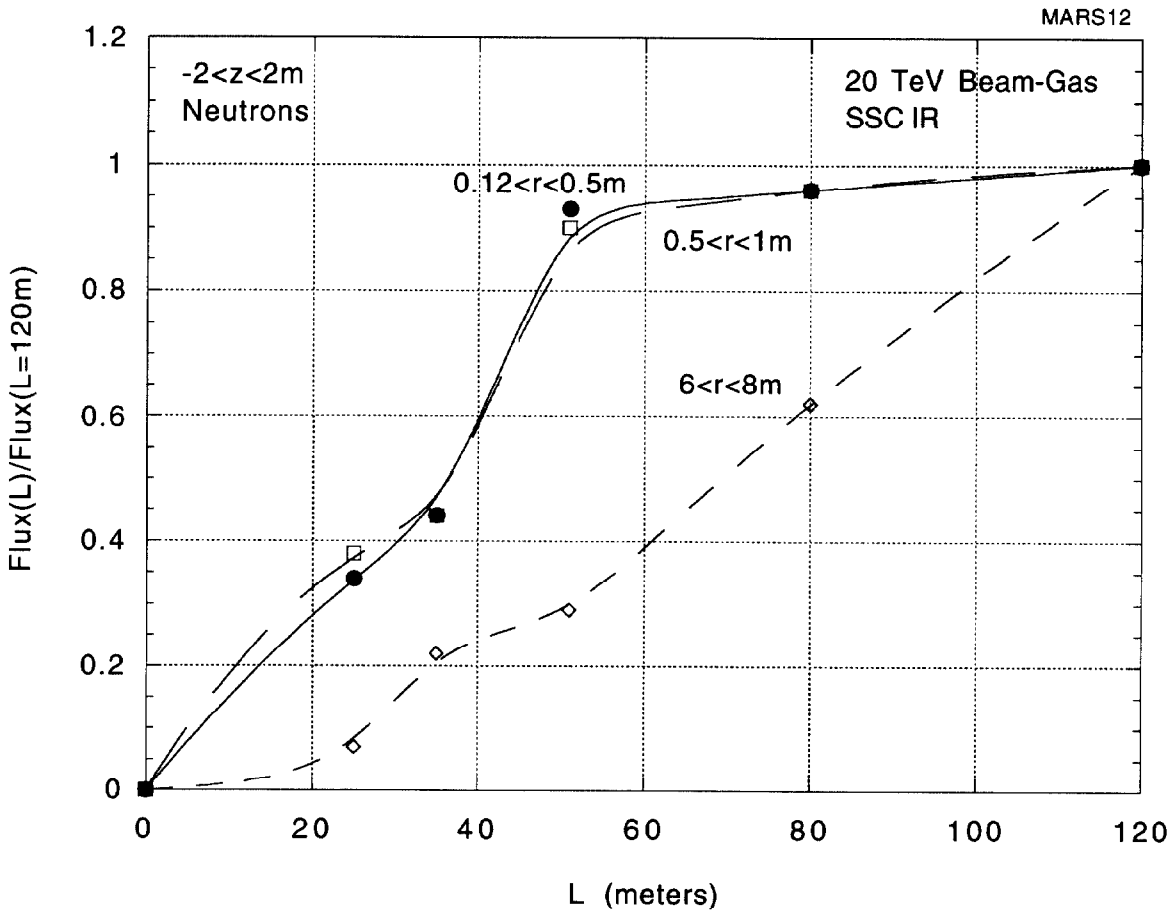
MARS12
-2<z<2m
Neutrons
20 TeV Beam-Gas
SSC IR
0.12<r<0.5m
0.5<r<1m
6<r<8m
Flux(L)/Flux(L=120m)
L (meters)
0
0.2
0.4
0.6
0.8
1
1.2
0
20
40
60
80
100
120

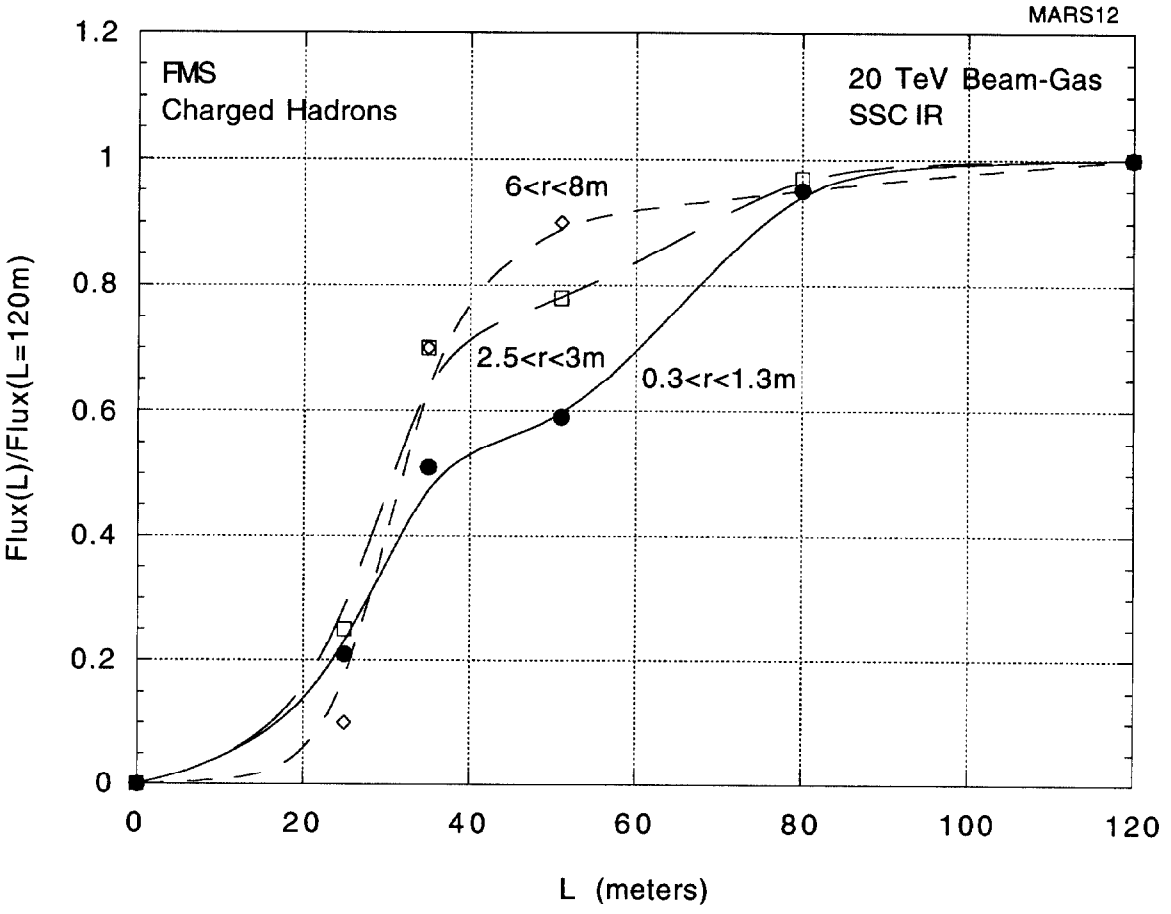
MARS12
FMS
Charged Hadrons
20 TeV Beam-Gas
SSC IR
6<r<8m
2.5<r<3m
0.3<r<1.3m
Flux(L)/Flux(L=120m)
L (meters)
0
0.2
0.4
0.6
0.8
1
1.2
0
20
40
60
80
100
120

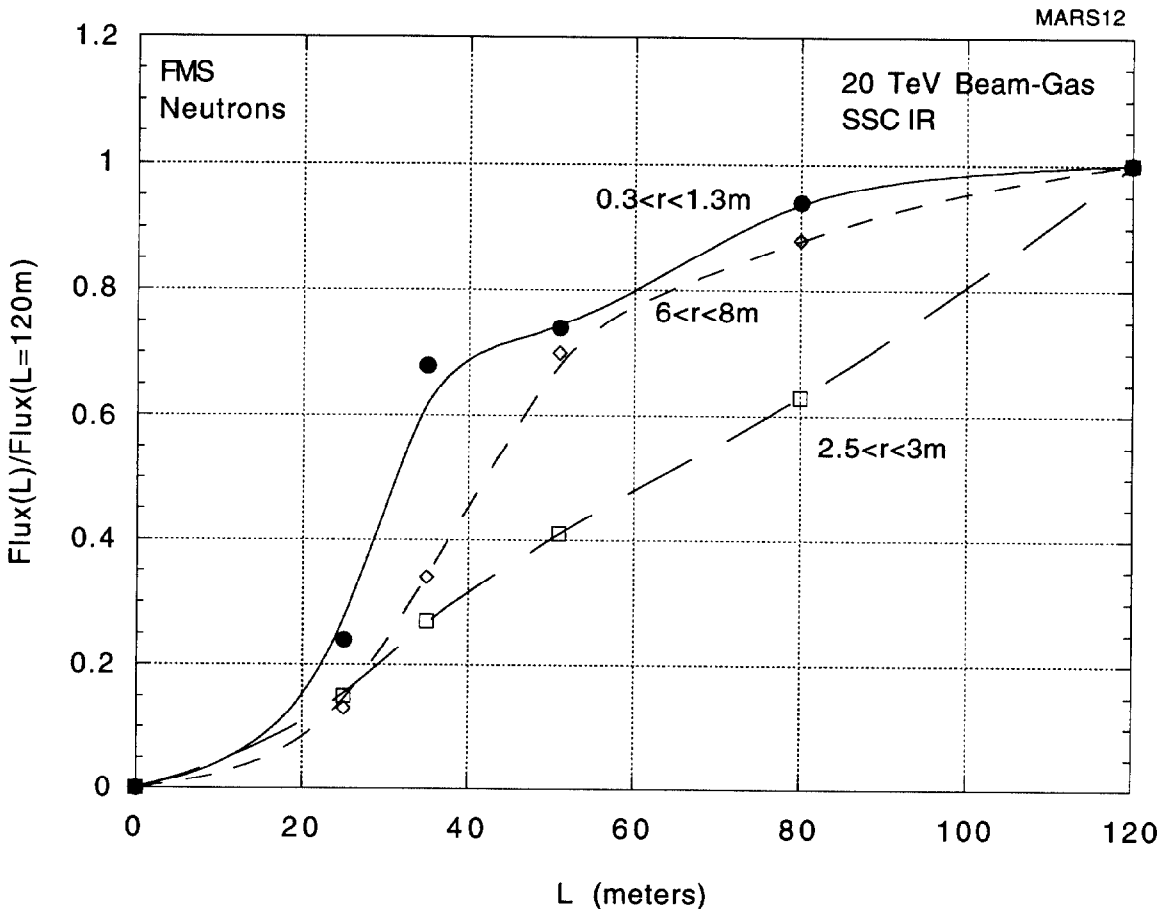
MARS12
FMS
Neutrons
20 TeV Beam-Gas
SSC IR
0.3<r<1.3m
6<r<8m
2.5<r<3m
Flux(L)/Flux(L=120m)
L (meters)
0
0.2
0.4
0.6
0.8
1
1.2
0
20
40
60
80
100
120

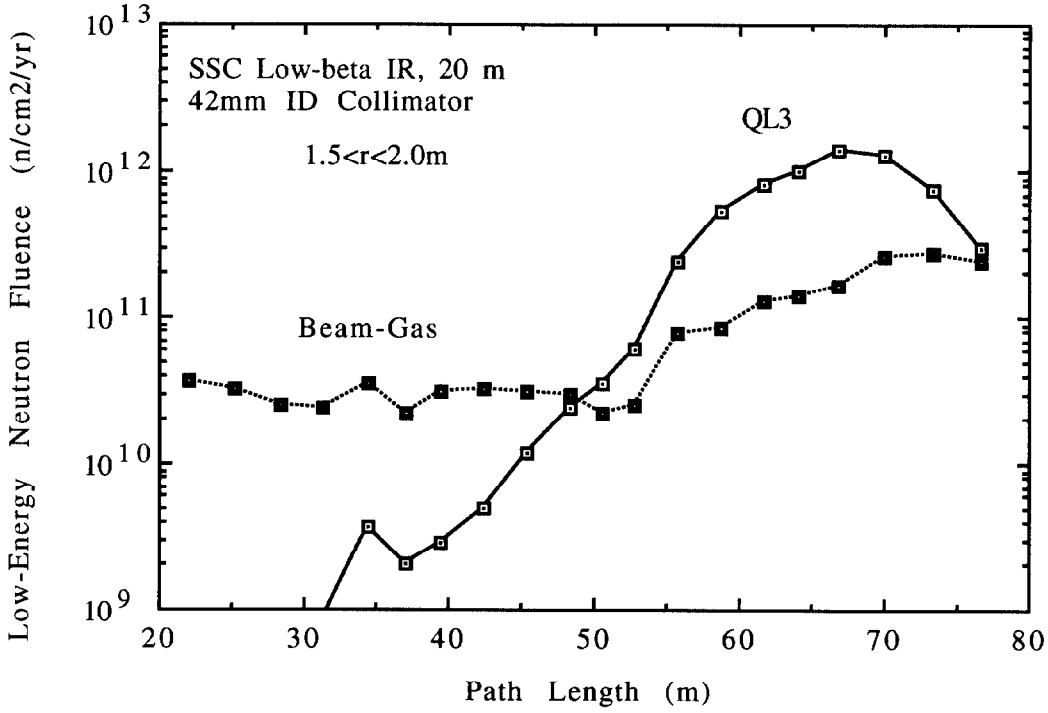
SSC Low-beta IR, 20 m
42mm ID Collimator
1.5<r<2.0m
QL3
Beam-Gas
Low-Energy Neutron Fluence (n/cm2/yr)
Path Length (m)
10^13
10^12
10^11
10^10
10^9
20
30
40
50
60
70
80

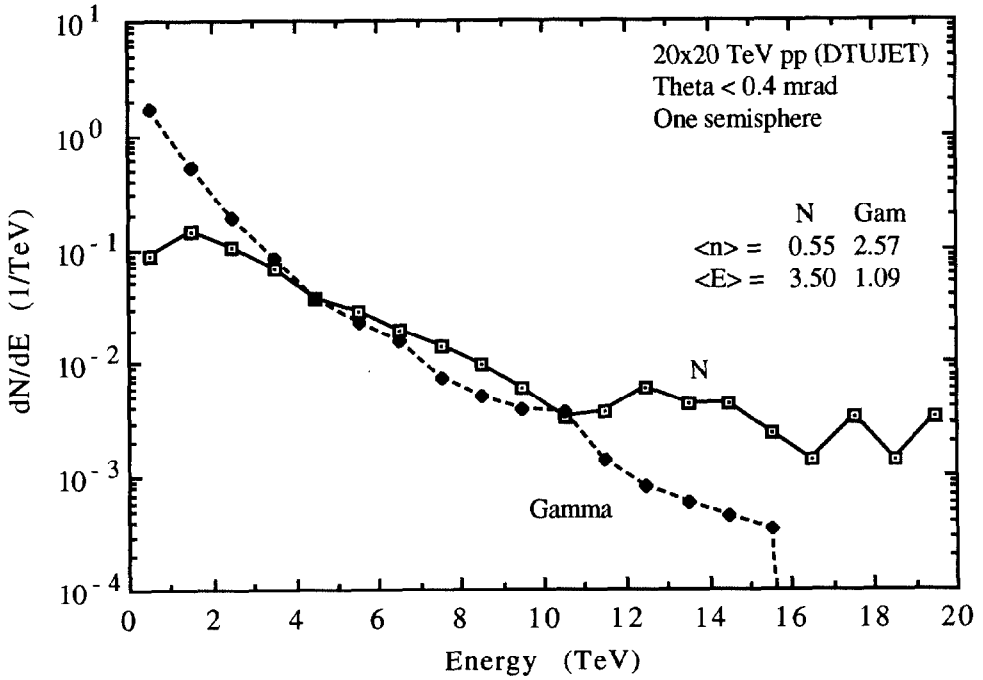
20x20 TeV pp (DTUJET)
Theta < 0.4 mrad
One semisphere
N Gam
<n> = 0.55 2.57
<E> = 3.50 1.09
N
Gamma
dN/dE (1/TeV)
Energy (TeV)
10^1
10^0
10^-1
10^-2
10^-3
10^-4
0 2 4 6 8 10 12 14 16 18 20

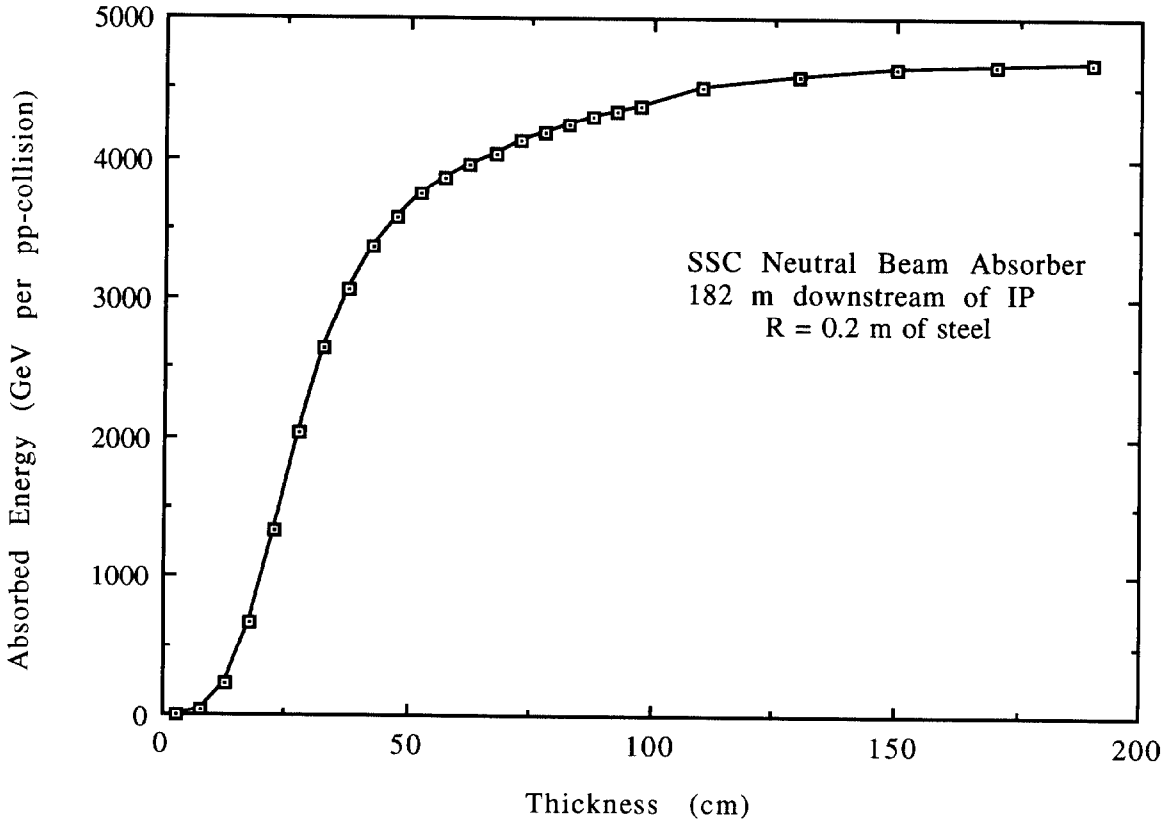
Absorbed Energy (GeV per pp-collision)
5000
4000
3000
2000
1000
0
0
50
100
150
200
Thickness (cm)
SSC Neutral Beam Absorber
182 m downstream of IP
R = 0.2 m of steel

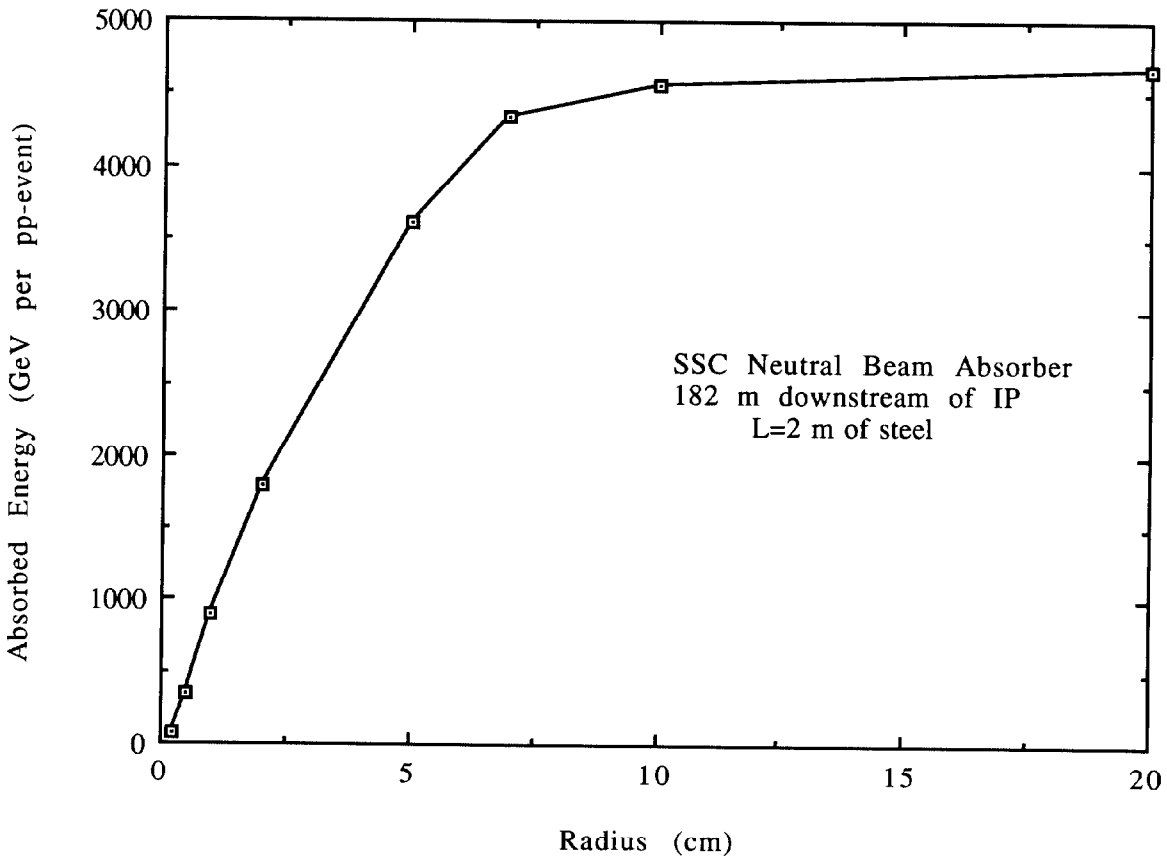
5000
4000
3000
2000
1000
0
Absorbed Energy (GeV per pp-event)
0
5
10
15
20
Radius (cm)
SSC Neutral Beam Absorber
182 m downstream of IP
L=2 m of steel

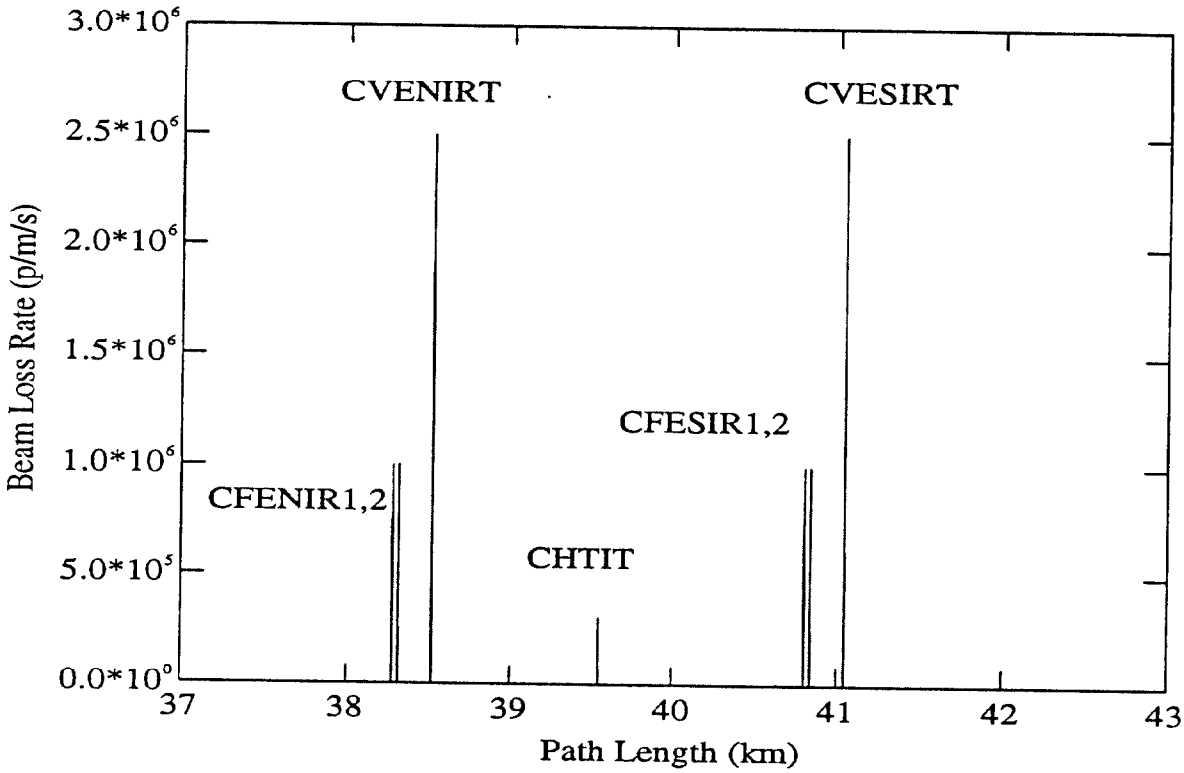
3.0*10^6
2.5*10^6
2.0*10^6
1.5*10^6
1.0*10^6
5.0*10^5
0.0*10^0
Beam Loss Rate (p/m/s)
CVENIRT
CVESIRT
CFESIR1,2
CFENIR1,2
CHTIT
37
38
39
40
41
42
43
Path Length (km)